Comparison of Global Diabatic Heating Rates from FGGE Level IIIb Analyses with Satellite Radiation Imagery Data

AKIRA KASAHARA AND ARTHUR P. MIZZI

National Center for Atmospheric Research,* Boulder, Colorado 80307

U. C. MOHANTY

Indian Institute of Technology, New Delhi, India

ABSTRACT

We evaluate the global distribution of diabatic heating rates based on the thermodynamic energy budget using the ECMWF Level IIIb FGGE analyses. We select the two 15-day periods of 27 January to 10 February 1979, during the FGGE Special Observing Period (SOP)-I, and 7-21 June 1979, in the SOP-II. An effort is made to examine the daily variation of tropospheric diabatic heating in contrast with previous investigations which dealt with the climatological aspect. The daily variations of tropospheric diabatic heating appear to be related to synoptic features of the global circulation, indicating that the diagnosed heating distributions provide useful information related to numerical weather prediction. Nevertheless, a question may be raised regarding the accuracy of the daily variations of diagnosed heating rates, since the calculation of diabatic heating involves an observationally sensitive quantity, i.e., the vertical motion.

One way to investigate the accuracy of diagnosed heating rates is to compare the present results with similar calculations using different FGGE datasets. In the Appendix, we present the diagnosed heating rates based on the GFDL Level IIIb data for the SOP-I study period. While comparisons of heating rates calculated from different analyses are revealing, we still lack an independent measure of comparison. We propose, therefore, the use of infrared and visible radiometric imagery data from the TIROS-N to examine the reliability of diagnosed heating and vertical velocity distributions in the tropics. A stratification of radiance data in terms of cloud types helps to establish useful relationships between infrared radiance and diabatic heating (and vertical velocity), suggesting that radiance data may be used to infer the distribution of diabatic heating in the tropics and to improve the analysis of the divergent wind field.

1. Introduction

The effects of physical processes in the atmosphere are ordinarily considered secondary in obtaining balanced initial conditions of velocity and mass (pressure or temperature) for primitive equation models. This may be partly due to the general belief that the problem of initialization is looked upon as a dynamical process involving adjustment between quasi-geostrophic and gravity wave motions. Also, forecasters have been concerned with predicting disturbances mostly in the midlatitudes where atmospheric baroclinicity is strong and provides a major mechanism for the conversion of potential energy to kinetic energy. Adiabatic initialization schemes are generally considered satisfactory in the midlatitudes.

This traditional view of initialization is deficient when we are interested in predicting the global atmosphere. It is well known that application of adiabatic initialization schemes suppresses the Hadley–Walker

circulations in the tropics (Bengtsson, 1981). This shortcoming is consistent with the notion that the tropical atmosphere tends to be barotropic in the absence of diabatic heating. Adiabatic initialization schemes produce only a weak vertical circulation, since the Hadley and Walker circulations are thermally forced (e.g., Gill, 1980). In order to retain features of both stationary and transient tropical motions, it is essential to incorporate the effects of diabatic heating into initialization schemes. Hence, knowledge of the global distribution of diabatic heating is important not only for climate research, but also for initializing primitive equation prediction models.

Long-term mean (on the order of one month or more) global patterns of diabatic heating rate have been studied using analyzed data during the Global Weather Experiment or First GARP Global Experiment (FGGE) of 1979. Wei et al. (1983) and Johnson et al. (1985) calculated climatological diabatic heating distributions using the FGGE Level IIIa analyses produced by the National Meteorological Center. They calculated diabatic heating rates from the mass continuity equation in isentropic coordinates. Masuda (1984) and Ka-

---

sahara and Mizzi (1985) evaluated the global distribution of diabatic heating as a residual of the thermodynamic energy equation in pressure coordinates using the FGGE Level IIIb analyses produced by the European Centre for Medium Range Weather Forecasts (ECMWF). Boer and Sargent (1985) calculated the vertically integrated fluxes of mass and energy using ECMWF Level IIIb analyses and determined the time average global heating rates for January and July 1979. Chen and Baker (1986) used the FGGE IIIb analyses of the Goddard Laboratory for Atmospheres (GLA) for their global diabatic heating calculations. More recently, efforts have been made to compare the results of diabatic heating calculations from different FGGE datasets for the same period in order to evaluate the accuracy of heating calculations. For example, Holopainen and Fortelius (1986) compared the global diabatic heating rates for February 1979 from two FGGE Level IIIb analyses prepared by ECMWF and GLA. For their one-month study period, the zonal mean of the two heating calculations agree particularly well. Boer (1986) investigated global mass and energy budgets for July 1979 using two FGGE Level IIIb analyses produced by the Geophysical Fluid Dynamics Laboratory (GFDL) and by ECMWF. Boer's calculations show rather marked differences between diabatic heating rates from the two FGGE datasets, although the broad features are in agreement.

One difficult aspect of diabatic heating calculations by the energy or heat budget is the evaluation of the vertical energy transport. In particular, we must ask whether or not we can determine the vertical motion with sufficient accuracy from the analyzed wind field. The general impression from pre-FGGE studies, e.g., Newell et al. (1969), is that the vertical motion determined from the analyzed divergence field is not sufficiently accurate for calculation of diabatic heating.

The availability of FGGE Level III analyses produced from various analysis centers has provided an opportunity to examine the reliability of the vertical motion calculated from the observed wind field. Many investigators (e.g., Krishnamurti and Ramanathan, 1982; Paegle and Baker, 1982; Murakami and Ding, 1982; and Lorenc, 1984) feel that the analyzed (Level III) large-scale divergence field in the tropics contains significantly more usable information than previously believed observable. However, a question has been raised as to how accurate the analysis is of the divergent wind field. For example, Julian (1985) indicates that a significant disparity exists among the analyses of divergent wind, produced by the various analysis centers, for scales smaller than approximately zonal wavenumber 10. The fact that long-term heating rates obtained by various investigators show gross agreement implies that the time averaged (on the order of one month) vertical motion is reliable. However, little is known about the accuracy of the diabatic heating rate and the vertical motion field on a daily basis.

In this study, we investigate the global distributions of diabatic heating during two 15-day periods in the Special Observing Periods (SOP) I and II of the FGGE year 1979. In contrast with the aforementioned investigations of diabatic heating, our study emphasizes the daily change of tropospheric diabatic heating rates rather than the climatological aspect. We are interested in the determination of global diabatic heating rates from the standpoint of application to numerical weather prediction.

Although diabatic nonlinear normal mode initialization (NNMI) schemes are now employed at operational forecasting centers, the initial specification of the divergence field appears to remain unsatisfactory due partly to deficiencies in the diabatic heating rates which are used in NNMI (Puri, 1985; Mohanty et al., 1986). The diabatic heating rates are generally computed from a two-hour model integration starting from uninitialized data. Solar heating and infrared cooling rates are calculated by the model's radiative formulations with sufficient accuracy dependent upon the cloud parameterizations. Similarly, the sensible heat flux from the earth's surface and the release of latent heat from nonconvective clouds are usually calculated satisfactorily. However, the release of latent heat from deep convection, particularly in the tropics, is grossly underestimated (or overestimated in some cases) during the first several hours of a forecast run. This spinup problem appears in all forecast models, including operational ones (Girard and Jarraud, 1982; Heckley, 1985). Therefore, it is important to diagnose global diabatic heating rates correctly from synoptic data for comparison with the model generated heating rates. [An alternative is to calculate diabatic heating rates during a continuous data assimilation to avoid the spinup problem. For example, Schubert and Herman (1981) calculated the global diabatic heating rates as a by-product of four-dimensional data assimilation by sampling the heating rates at 6 to 9 hours after the insertion of synoptic observations into a general circulation model.]

In section 2, we describe the computing schemes and data used in this study. In section 3, we present the diagnosed global heating distributions for the SOP-I study period, 27 January to 10 February 1979, using the ECMWF Level IIIb dataset. The calculations for the same period are repeated with the GFDL Level IIIb analyses and the results are presented in the Appendix for comparison. In section 4, we present the results for the SOP-II study period, 7–21 June 1979.

While the comparisons of heating rates calculated from different FGGE datasets are useful, we still lack an independent measure of comparison. A number of investigations have been made to indirectly estimate rainfall rates using visible and/or infrared radiation imagery from satellites (e.g., Krishnamurti et al., 1983). Since tropical heating areas are mostly associated with the release of latent heat of condensation and/or the

transfer of sensible heat from the warm surfaces of the earth, and cooling areas generally do not have clouds, it may be useful to compare heating/cooling patterns with visible and infrared radiation imagery data taken from satellites. In section 5, we present a comparison of our diagnosed heating rates with visible and longwave radiation imagery data taken from the polar-orbiting TIROS-N satellite. Discussion of these comparisons is presented in section 6.

2. Computing schemes and data

The daily global diabatic heating rates are calculated as a residual of the thermodynamic equation. We adopt the form of the thermodynamic energy equation given in the National Center for Atmospheric Research (NCAR) Community Climate/Forecast Model, version zero B (CCM0B):

$$\frac{\partial T'}{\partial t} + \frac{1}{a\cos^2\phi}\frac{\partial}{\partial\lambda}(uT'\cos\phi) + \frac{1}{a\cos\phi}\frac{\partial}{\partial\phi}(vT'\cos\phi)$$

$$- T'\delta + \dot{\sigma}\frac{\partial T}{\partial\sigma} + \kappa\frac{T\omega}{p} = \frac{Q}{C_p}, \quad (2.1)$$

where λ, ϕ, σ and t denote, longitude, latitude, vertical coordinate ($\sigma = p/p_s$ with the pressure p and the surface pressure p_s), and time. The velocity components are u (eastward), v (northward), and $\dot{\sigma}$ ($=d\sigma/dt$). A mean radius of the earth is given by a. The temperature T is divided into two parts:

$$T = T' + T_0(\sigma), \quad (2.2)$$

where $T_0(\sigma)$ represents a global average temperature which depends only on σ. In (2.1), $\kappa = R/C_p$, where R is the gas constant for dry air and C_p denotes the specific heat of dry air at constant pressure. The horizontal divergence δ and pressure vertical velocity ω ($=dp/dt$) are calculated from

$$\delta = \frac{1}{a\cos\phi}\left[\frac{\partial u}{\partial\lambda} + \frac{\partial}{\partial\phi}(v\cos\phi)\right], \quad (2.3)$$

$$\omega = p\left[\mathbf{V}\cdot\nabla\ln p_s - \frac{1}{\sigma}\int_0^\sigma(\delta + \mathbf{V}\cdot\nabla\ln p_s)d\sigma\right]. \quad (2.4)$$

The numerical approximations and computational procedures are described in a series of NCAR technical reports (Williamson, 1983; Williamson et al., 1983; Sato et al., 1983).

We use (2.1) to diagnose diabatic heating. All terms on the left-hand side are evaluated using analyzed data, and the heating rate on the right-hand side is the resulting residual. The temperature tendency $\partial T'/\partial t$ in (2.1) is calculated as the finite difference $\Delta T'/\Delta t$ computed from the difference in T' at 1200 UTC and at 1200 UTC the following day ($\Delta t = 24$ h). This temperature tendency is regarded as an average within the 24-h interval. The remaining five terms on the left-hand side of (2.1) are calculated at 1200 UTC and at

1200 UTC the following day. Then, these five terms at the two consecutive time levels are arithmetically averaged to obtain their mean values for the 24-h interval. The right-hand side Q/C_p is the sum of the six terms on the left and represents an average diabatic heating rate for the 24-h interval.

As calculated, these daily diabatic heating rates contain small-scale noise due to errors in the analyzed velocity and temperature fields. Also, in view of the discrepancy in the analysis of the divergent wind, as discussed in the Introduction, it is likely that only the large-scale part of the diabatic heating rates is meaningful. Since we are interested in the daily variation of diabatic heating, we wish to examine the scales of heating at higher resolution than those retained by most of the aforementioned climatological studies. After some experimentation, we adopted a spectral smoother which retains the first 13 wavenumber components, including wavenumber zero, in a triangular spherical harmonics expansion.

To perform the diabatic heating rate calculations, we use the ECMWF Level IIIb gridded (uninitialized) fields of u, v and T at the 15 standard pressure levels with a horizontal resolution of 1.875° on a latitude-longitude grid. The 1200 UTC data at pressure levels are linearly interpolated from $\log\sigma$ surfaces to the σ levels presented in Table 1. Finally, the data on each σ-level are interpolated using bicubic Lagrangian polynomials onto the Gaussian grid of the CCM0B (7.5° longitude and 40 latitude points).

We selected the two 17-day periods of 26 January–11 February 1979, during the FGGE Special Observing Period-I (SOP-I), and 6–22 June 1979, in the SOP-II. However, the diagnosed heating rates apply to the 15-day periods of 27 January–10 February 1979, and of 7–21 June 1979, due to the averaging procedure described previously. Although the heating rates are calculated at all σ-levels, we found the results of the two uppermost levels to be unrealistic. This may be due to a combination of stratospheric analysis error and computational error resulting from coarse vertical resolution near the upper part of our grid. In any case, we ignore the results at the σ-levels 1 and 2 in our presentation.

TABLE 1. Location of σ_k-levels and the thickness of layer $\Delta\sigma_k$ representing σ_k at the middle of each layer used in the heating calculations.

Index k	σ_k	$\Delta\sigma_k$
1	0.009	0.042
2	0.074	0.090
3	0.189	0.131
4	0.366	0.156
5	0.500	0.164
6	0.664	0.156
7	0.811	0.131
8	0.926	0.090
9	0.991	0.042

3. Global distribution of heating rates for SOP-I study period

In presenting our results, the 15-day period of 27 January to 10 February 1979, is referred to as the SOP-I study period. Figures 1a–g show the patterns of Q_k/C_p averaged during the SOP-I study period at σ_k levels, $k = 9$ to 3, where subscript k denotes the index of the σ-level shown in Table 1. The contour intervals are 2 $\times 10^{-5}$ K s^{-1} (≈ 1.7 K day^{-1}).

One feature which stands out clearly is a strong heating maximum off the east coast of North America. The maximum heating of 16 K day^{-1} appears at the lowest level (Fig. 1a) and the heating rates gradually decrease upward (in units of K day^{-1}, 15 at σ_8, 11 at σ_7, 7 at σ_6, 7.5 at σ_5, and 7 at σ_4). This heating maximum appears to be related to the presence of an intense western Atlantic low which persisted during the study period, accompanying the advection of cold arctic air across most of the United States east of the continental divide. Near-record cold persisted over the Northeast (Dickson, 1979). It is likely that this cold air advection from the North American continent to the Atlantic ocean created an intense source of sensible and latent heating over the western Atlantic.

A similar situation can be seen off the east coast of Asia. The maximum heating of 9 K day^{-1} at the lowest level (Fig. 1a) tends to decrease upward, suggesting that the source of heating is due to the transport of sensible heat and moisture from the ocean.

Another heating maximum is seen over the Tibetan Plateau and the heating rates reach a maximum of 6 K day^{-1} around σ_5 (Fig. 1e). While cooling prevails over the Eurasian continent during the study period, the Tibetan Plateau acts as an elevated heat source. As discussed in the Appendix, this feature is absent from the GFDL results providing a major discrepancy between the diagnosed heating rates from the ECMWF and GFDL analyses. Since studies conducted in the People's Republic of China indicate that the atmosphere above the Tibetan Plateau is cooling during winter (e.g., Reiter and Gao, 1982), it is likely that the ECMWF result is unrealistic in this respect.

We see heating areas over Alaska and the Bering Strait. A maximum heating of 7 K day^{-1} appears at the lowest level and decreases sharply upward. The source of heating is likely the transport of sensible and latent heat to the atmosphere from the sea. Similarly, heating takes place south of Greenland. We see moderate heating rates in the lower troposphere which intensify in the upper troposphere. This appears to be related to the fact that the west Atlantic low discussed earlier slowly moved northeastward in the latter part of the study period and further developed.

Another heating maximum is seen over the Sahara desert. Although the heating rates are strongest near the surface, substantial heating occurs at the upper levels as well. The GFDL results indicate heating

throughout the troposphere with a maximum at the $\sigma = 0.811$ level. Over the highlands of South Africa, fairly intense heating exists. The heating rates are uniform throughout the troposphere. As we discuss in section 5, this heating area coincides with a low infrared temperature area in radiation imagery data of NOAA TIROS-N, suggesting that the source of heating is the release of latent heat of condensation in deep cumulus convection.

Similar situations are seen in the heating areas over South America, Brazil, and the east coast of South America. Heating over the Amazon basin is associated with a large-scale convective system which is characterized by low-level convergence and upper-level divergence. Heating over the east coast of South America around 35°S is associated with a midlatitude trough. Actually these two heating areas are connected, as can be seen clearly from motion pictures of cloud movement taken from the GOES-East geostationary satellite during the period. This combined tropical anticyclone-midlatitude trough system is a familiar feature of summer circulations over South America (Virji, 1981; Kousky and Gan, 1981).

Other convectively driven heating areas are seen over the East Indies extending east of the dateline. The heating rates in this equatorial zone increase upward and are very intense in the upper troposphere. The heating distribution in this area agrees well with the convective index pattern of Murakami (1983), indicating that the source of heating is deep moist convection.

In the Southern Hemisphere, at the lowest level (Fig. 1a), intense heating of 11 K day^{-1} is seen off the southwest coast of Australia. The heating rates decrease rather sharply upwards. In the GFDL results (Fig. 17a), there is a heating maximum at the southern coast of Australia. Although the magnitudes differ, the fact that the GFDL heating rates decrease sharply upwards suggests that the source of heating is mostly the sensible heat transport from the ocean. This may be consistent with the observation, discussed in section 5, that the infrared temperatures obtained from TIROS-N measurements show no indication of deep convection there.

Broad areas of weak heating exist over the mid-South Pacific and the periphery of Antarctica in the eastern hemisphere. It appears that these heating areas coincide with storm tracks.

Generally, cooling takes place in the Arctic region and over the Eurasian continent. Also, cooling prevails over most of the Atlantic, except for the intense heating areas off the east coasts of North and South America mentioned earlier. Broad cooling over the eastern Pacific off the west coasts of North and South America is also well identified.

Figure 2a shows the 15-day average of the mass-weighted vertically averaged heating rates calculated from
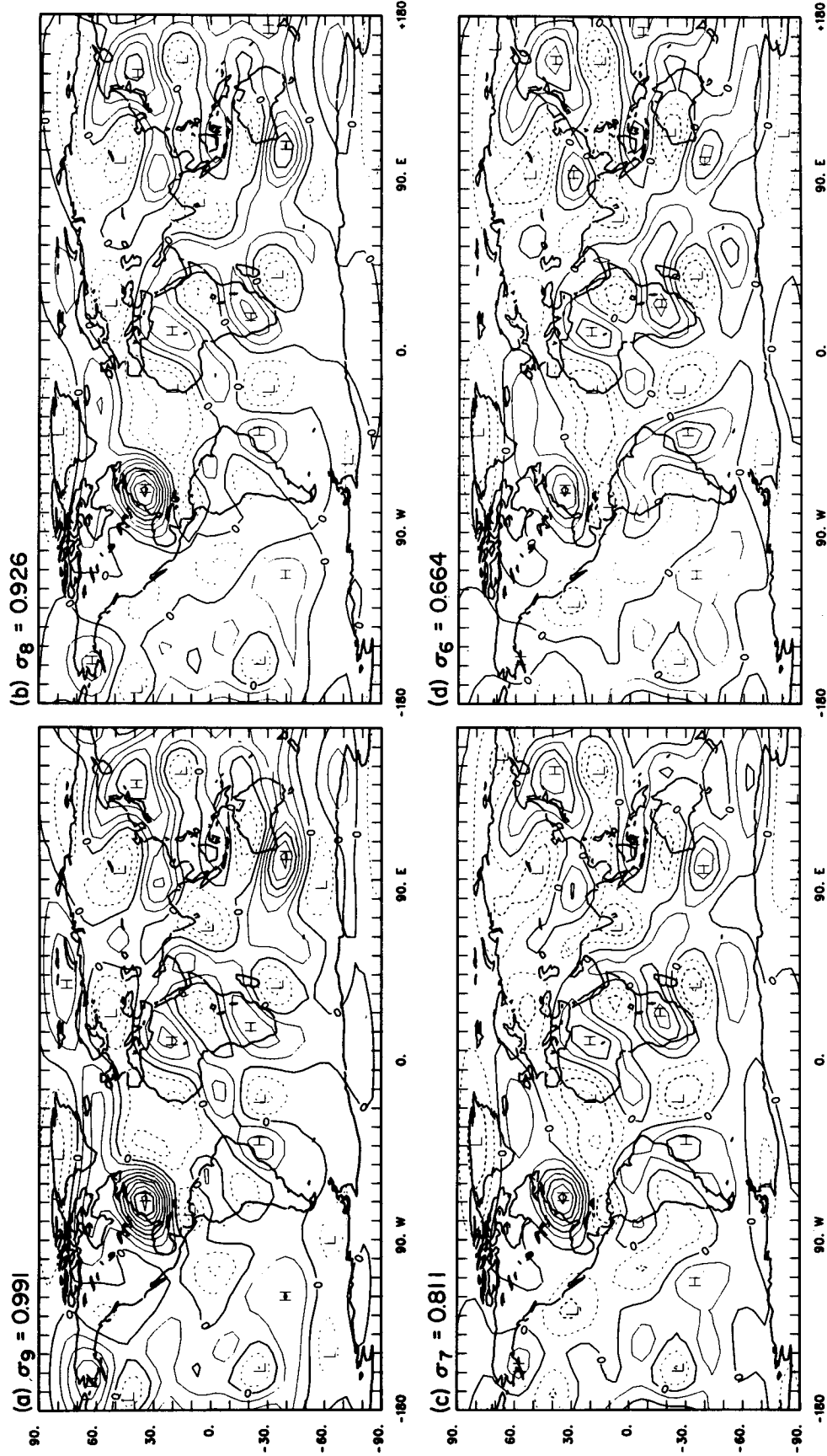
FIG. 1. Diabatic heating rates Q_k/C_p averaged during the SOP-I study period at σ_k-levels. Contour interval is 2×10^{-5} K s^{-1} (≈ 1.7 K day^{-1}). Solid (dashed) lines denote heating (cooling). (a) at $\sigma_9 = 0.991$, (b) at $\sigma_8 = 0.926$, (c) at $\sigma_7 = 0.811$, (d) at $\sigma_6 = 0.664$, (e) at $\sigma_5 = 0.500$, (f) at $\sigma_4 = 0.366$ and (g) $\sigma_3 = 0.189$.

FIG. 1. (Continued)

(a) SOP-I STUDY PERIOD
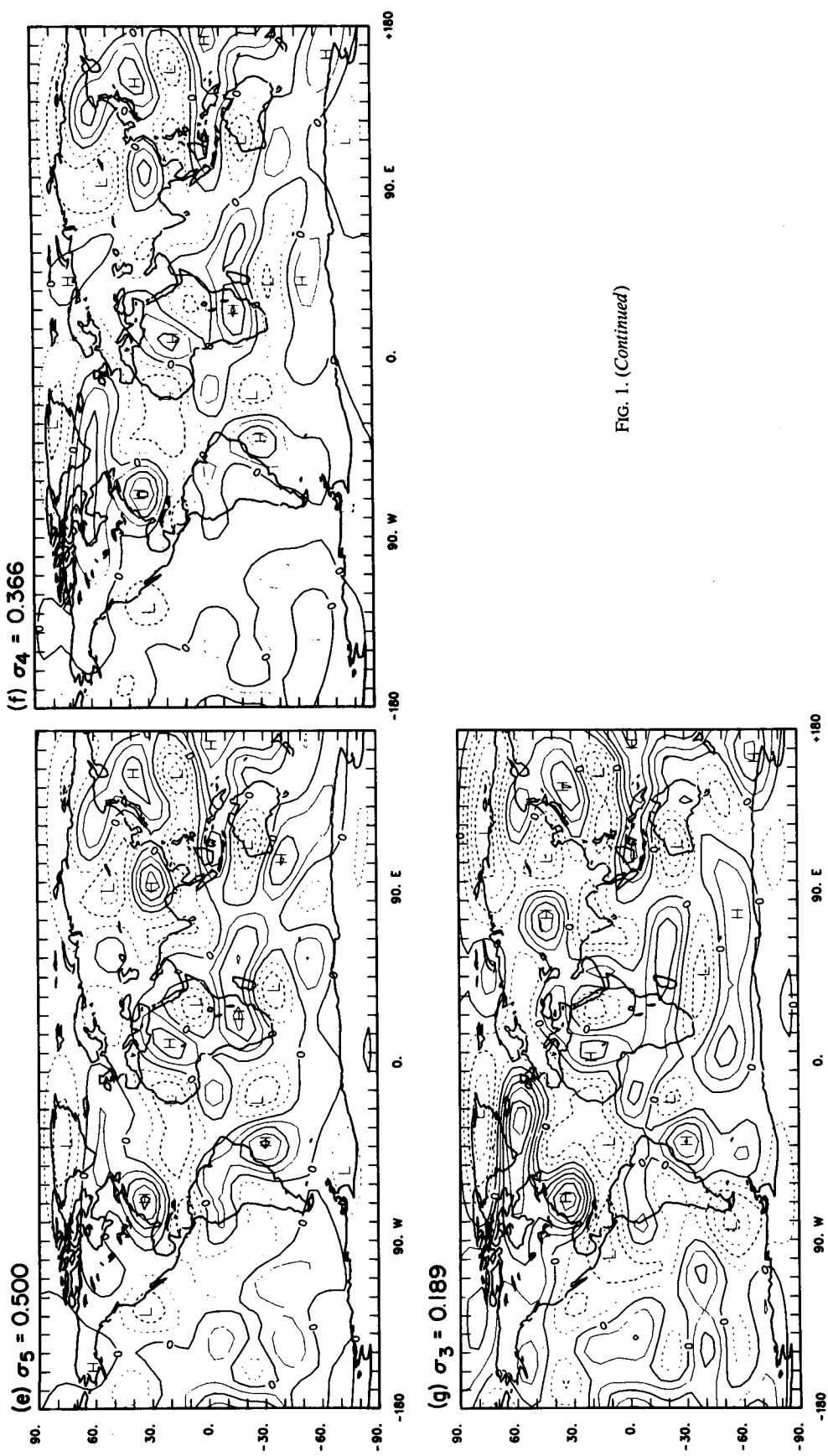
(b) SOP-II STUDY PERIOD
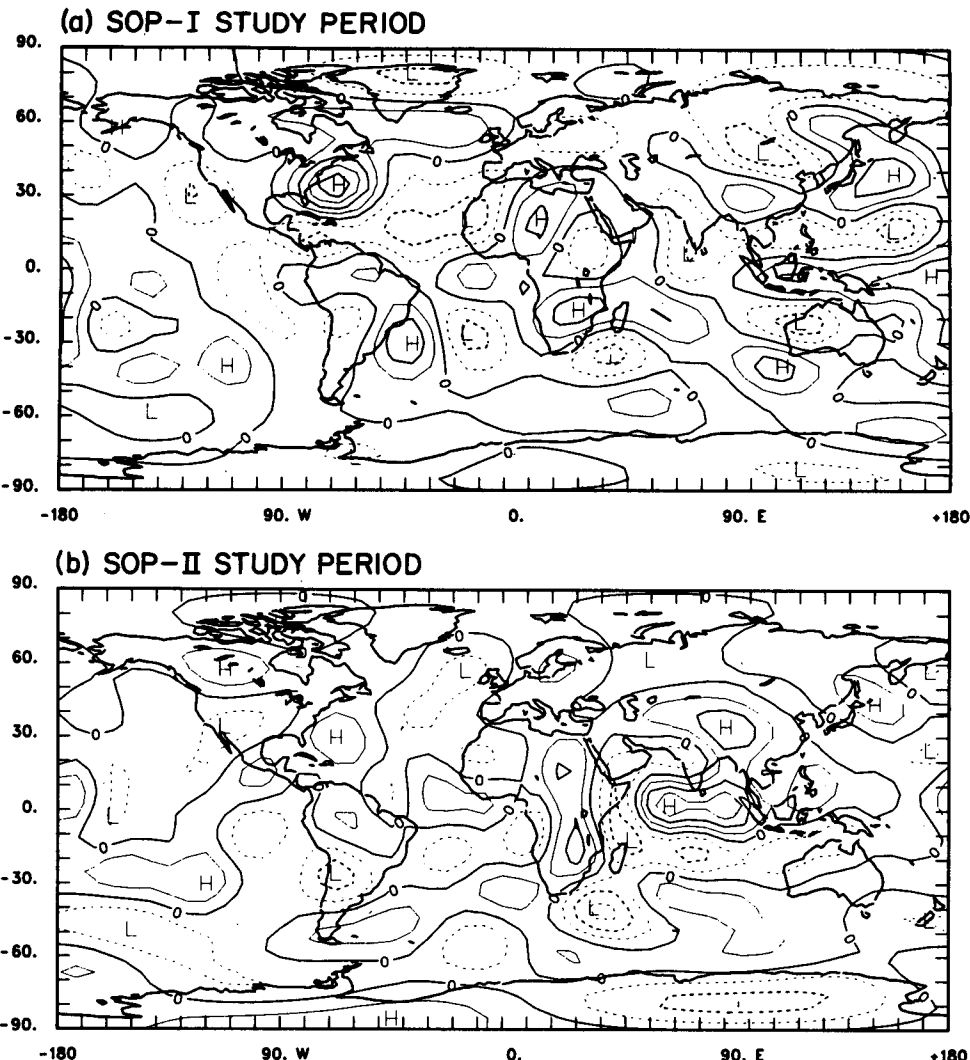
FIG. 2. Distributions of mass-weighted vertically averaged heating rate $\tilde{Q}/C_p$ defined by (3.1) averaged during: (a) SOP-I study period, 27 January to 10 February 1979; and (b) SOP-II study period, 7–21 June 1979. Contour interval is 2×10^{-5} K s^{-1}. Dashed lines show cooling.

$$\frac{\tilde{Q}}{C_p} = \frac{1}{C_p} \sum_{k=1}^{9} Q_k \Delta\sigma_k, \qquad (3.1)$$

where level index k and thickness $\Delta\sigma_k$ are given in Table 1. The contour interval is 2×10^{-5} K s^{-1} (≈ 1.7 K day^{-1}). In calculating the mass-weighted vertically averaged heating rates, we assumed that $Q_k = 0$ at σ_2 and σ_1 in order to avoid the contamination of the result by the unrealistic values as discussed earlier. Neglect of the upper levels leads to error in the vertical integral, but its contribution is less than the uncertainty of the result itself.

The notable features of Fig. 2a are similar to those discussed already. In summary, we see: 1) heating contrasts along the east and west coasts of North America and Eurasia; 2) areas of heating over the tropical western Pacific, north and south Africa, the central to south

Indian Ocean, and South America; and 3) areas of cooling over the eastern Pacific, the eastern Atlantic, Eurasia, and the Arctic region. The broad features of Fig. 2a agree fairly well with the December 1978–February 1979 cases shown in Wei et al. (1983) and Masuda (1984), the January 1979 cases in Johnson et al. (1985) and Boer and Sargent (1985), the 5 January–4 March 1979 case in Chen and Baker (1986), and the February 1979 cases in Holopainen and Fortelius (1986). However, at this stage detailed comparisons between the results from these various investigators are not very meaningful due to differences in the periods of analysis, the datasets used, and the methods of diagnosis. Recently, efforts have been made by Holopainen and Fortelius (1986), Boer (1986), and others to compare the results of heating calculations obtained by using different Level IIIb datasets with identical

computing schemes. In the Appendix, we provide pre-liminary comparison of our results from the ECMWF data with those from the GFDL data for the same period in order to assess the reliability of the heating calculations.

Since we are interested in examining day-to-day variations of the global heating distributions particularly in the tropics, we show in Fig. 3 a time series of the mass-weighted vertically averaged heating rates between 30°N to 30°S during the SOP-I study period. The contour interval is 2×10^{-5} K s^{-1}. Let us first follow the time variation of heating over South America. A heating maximum over the Amazon basin appears at the beginning (28–29 January), moves southeastward and intensifies over the east coast of South America (2–3 February). At the same time, heating develops over the west coast of South America (1–2 February) and then moves eastward. Heating over the Amazon basin and heating off the east coast of South America around 30°S are related through an intense midlatitude trough.

Another notable feature is the temporal variation of the heating pattern over Africa. Recall that there are two heating maxima over Africa as was seen on the time averaged picture of Fig. 2a. Actually, the temporal variations of these two centers are significant. We see that heating formed over the western Indian Ocean (31 January), moved slowly westward during 31 January–5 February and eventually weakened. Then, heating redeveloped over the Indian Ocean (4 February) and slowly moved westwards again. The area of intense heating over North Africa (2 February) seems to be a part of the intertropical convergence zone over the Atlantic. The temporal variation of this heating appears to be more spontaneous than that of the other areas of heating. Over the East Indies, the heating zone appears stationary, while its intensity pulsates significantly.

The overall impression from Fig. 3 is that the temporal variation of large-scale heating in the tropics shows time continuity for the transient and stationary synoptic scale features. However, the question remains, to what extent are the temporal variations of diagnosed heating rates subject to observational and analysis errors. One way to answer this question is to compare Fig. 3 with Fig. 19 of the Appendix. The phenomenological descriptions of the temporal behavior of heating patterns over South America, Africa and the Indian Ocean are also applicable to Fig. 19, although one can find several differences between the two figures.

4. Global distribution of heating rates for SOP-II study period

We present the results of diabatic heating rates in the 15-day period of 7–21 June 1979 which is referred to as the SOP-II study period. Figures 4a–g show the same as Figs. 1a–g, except for the SOP-II study period.

The most notable feature in these figures is related to the summer monsoon over southeast Asia and is seen over the central Indian Ocean, the southwest Pacific and the eastern Tibetan Plateau. The broad area of heating from the East Indies to east of the dateline extends throughout the troposphere and agrees well with the convective index pattern for June 1979 shown in Murakami (1984). This heating area stretches westwards to the Indian Ocean. This feature is common throughout the σ-levels and coincides well with a low infrared temperature area in the radiation imagery data of TIROS-N (not shown). Hence, the heat source for this region is likely due to deep moist convection. Another salient feature of heating is seen over the eastern Tibetan Plateau. Again the vertical structure shows that the heating is almost uniform throughout the troposphere. It is likely that both deep moist convection and the transport of sensible heat are the sources of heating. Intense heating over the Indian Ocean is surrounded by relatively strong cooling over the Arabian Sea, off the east coast of central Africa and over the south Indian Ocean. These cooling areas coincide with relatively high infrared temperature areas in the TIROS-N imagery data (not shown), corresponding to descending motion areas discussed in section 5.

Other areas of heating are seen over the intertropical convergence zones in the central Atlantic extending to South America and in the Pacific from Central America to the mid-South Pacific. The heating rates are fairly uniform throughout the troposphere, suggesting that the source of heating is deep moist convection.

Generally, heating prevails over the continents in the Northern Hemisphere and cooling takes place over the oceans. There are a few exceptions, however. Cooling exists over the western United States and heating exists over the northwest Pacific to the east of Japan.

The heating/cooling patterns in the middle latitudes of the Southern Hemisphere seem to be associated with synoptic systems. Cooling generally prevails over Antarctica.

Figure 2b shows the 15-day average of the mass-weighted vertically averaged heating rate distribution. It is the same as Fig. 2a, except for the SOP-II study period. The broad features of Fig. 2b agree with the June–August 1979 cases in Wei et al. (1983), and Masuda (1984), the July 1979 cases of Johnson et al. (1985), Boer and Sargent (1985), and Boer (1986), and the 1 June–31 July 1979 case in Chen and Baker (1986). In detail, however, there are many noticeable differences. For example, the most prominent feature of Fig. 2b is the intense convective heating zone over the central Indian Ocean which is surrounded by relatively intense cooling. Except for Chen and Baker (1986), this feature is not seen in the results of earlier studies. The presence of the intense convective heating zone over the central Indian Ocean agrees well with a low infrared temperature area in radiation imagery data of TIROS-N. Another aspect of the difference between
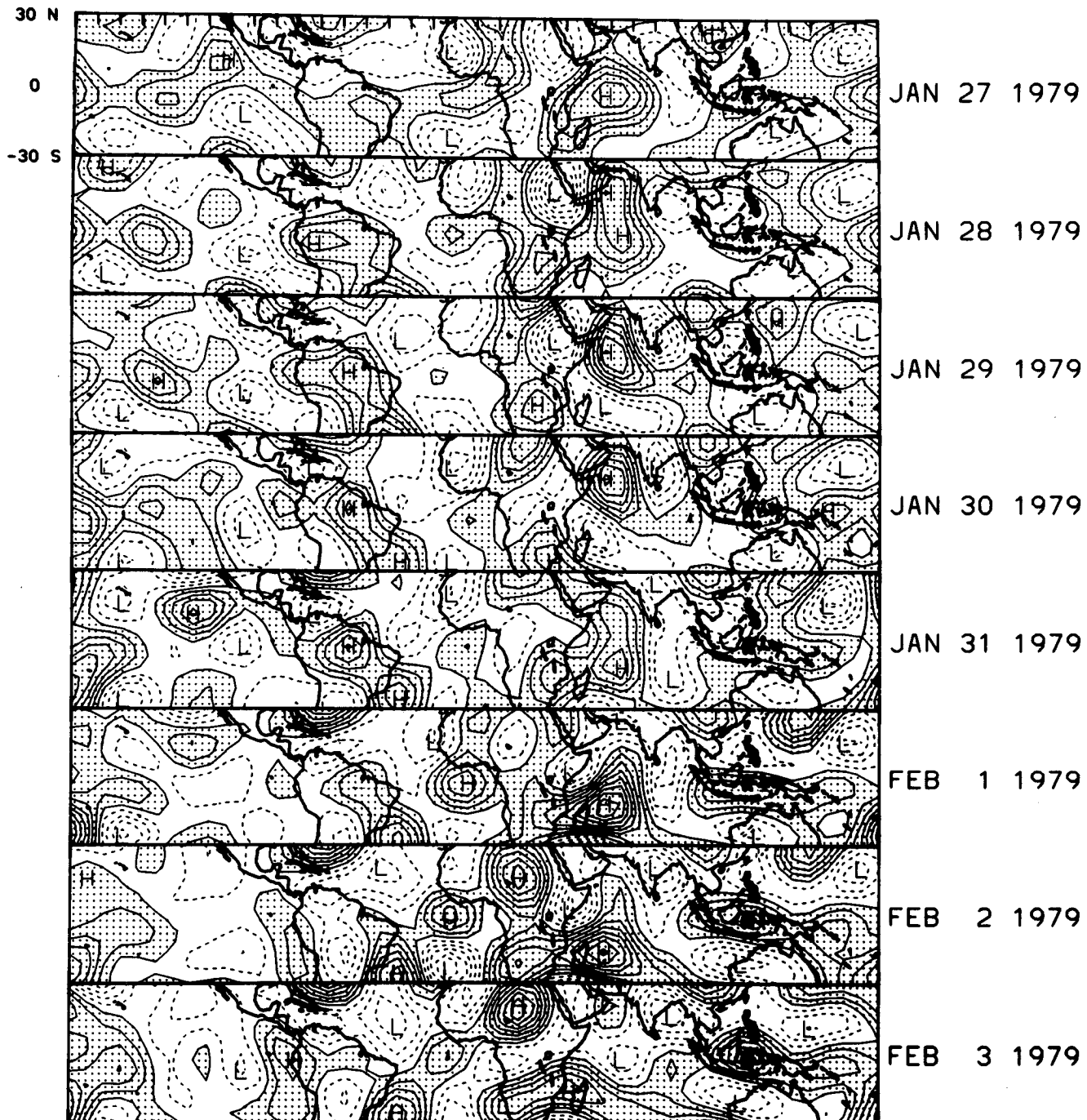
FIG. 3. Time series of mass-weighted vertically averaged heating rates between 30°N to 30°S during the SOP-I study period. Contour interval is 2×10^{-5} K s^{-1}. Stippling shows heating areas. Dashed lines for cooling.

our results and those of other investigators is the presence of relatively intense heating over Africa which stretches in the north–south direction. By looking at the TIROS-N radiation data, the heating area over southern Africa seems to be erroneous. We discuss this problem in section 5.

The SOP-II study period is characterized by a transition of the summer monsoon over Asia. The period between 11 and 17 June coincides with the onset of the Indian summer monsoon as seen from an explosive growth of kinetic energy of low-level flow (Mohanty et al., 1984). Figure 5 shows a time series of the mass-
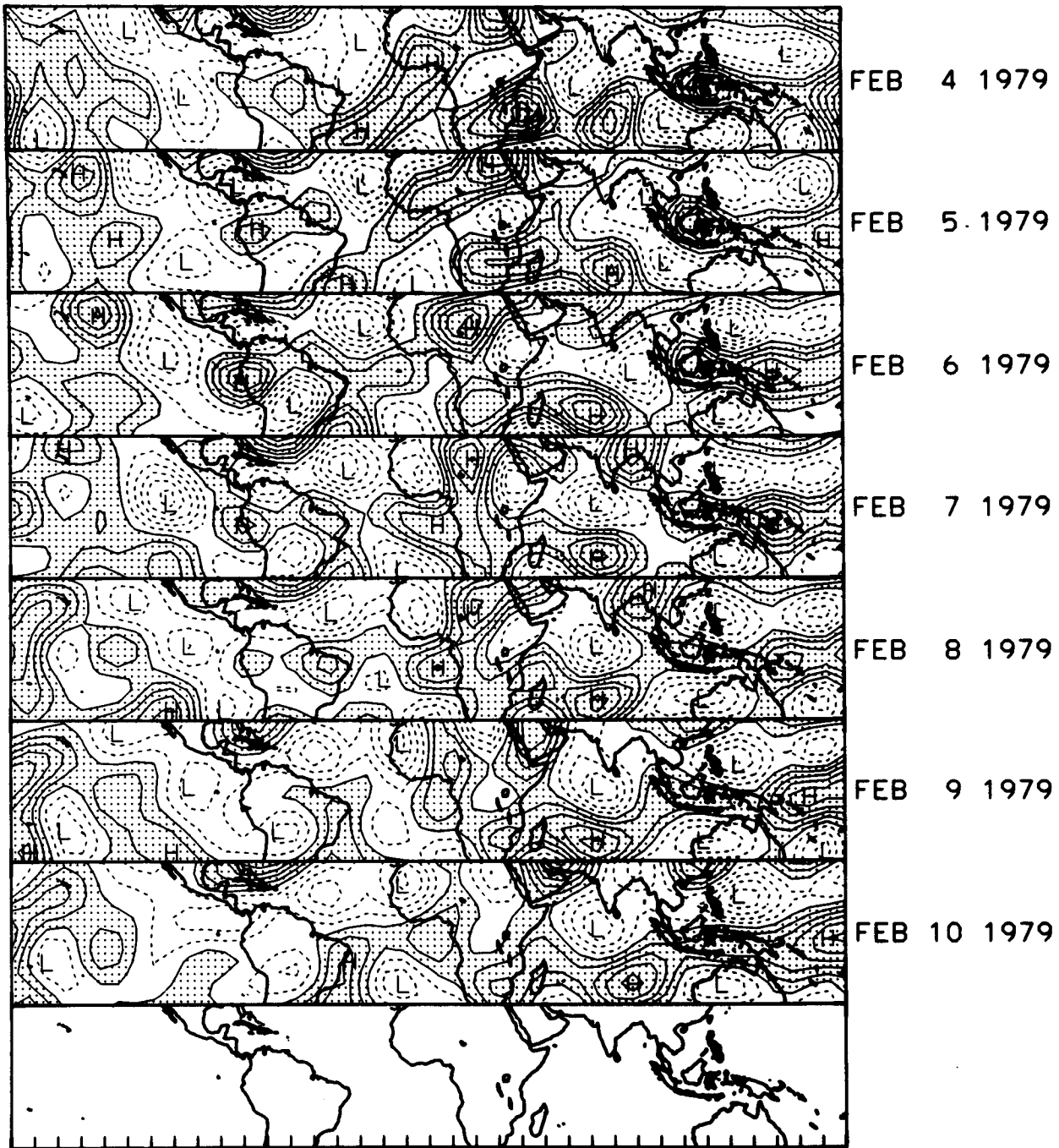
FIG. 3. (Continued)

weighted vertically averaged heating distributions between 30°N and 30°S. It is the same as Fig. 3, except for the SOP-II study period. One notable feature is the northward progression of the major heating area over the Indian Ocean. The heating rates increase dramatically during the period, 11–18 June. At the same time, the heating area moves gradually northward and reaches India, replacing the cooling region which pre-

vails over India at the beginning of this study period. The intensification and northward movement of the heating area coincide with the onset of the Indian summer monsoon. Moreover, the time evolution of heating during pre-onset, onset, and post-onset periods agrees in general with the analysis of heating presented by Krishnamurti and Ramanathan (1982).

Of course, not all aspects of the day-to-day variations

(a) $\sigma_9 = 0.991$

(b) $\sigma_8 = 0.926$

(c) $\sigma_7 = 0.811$

(d) $\sigma_6 = 0.664$
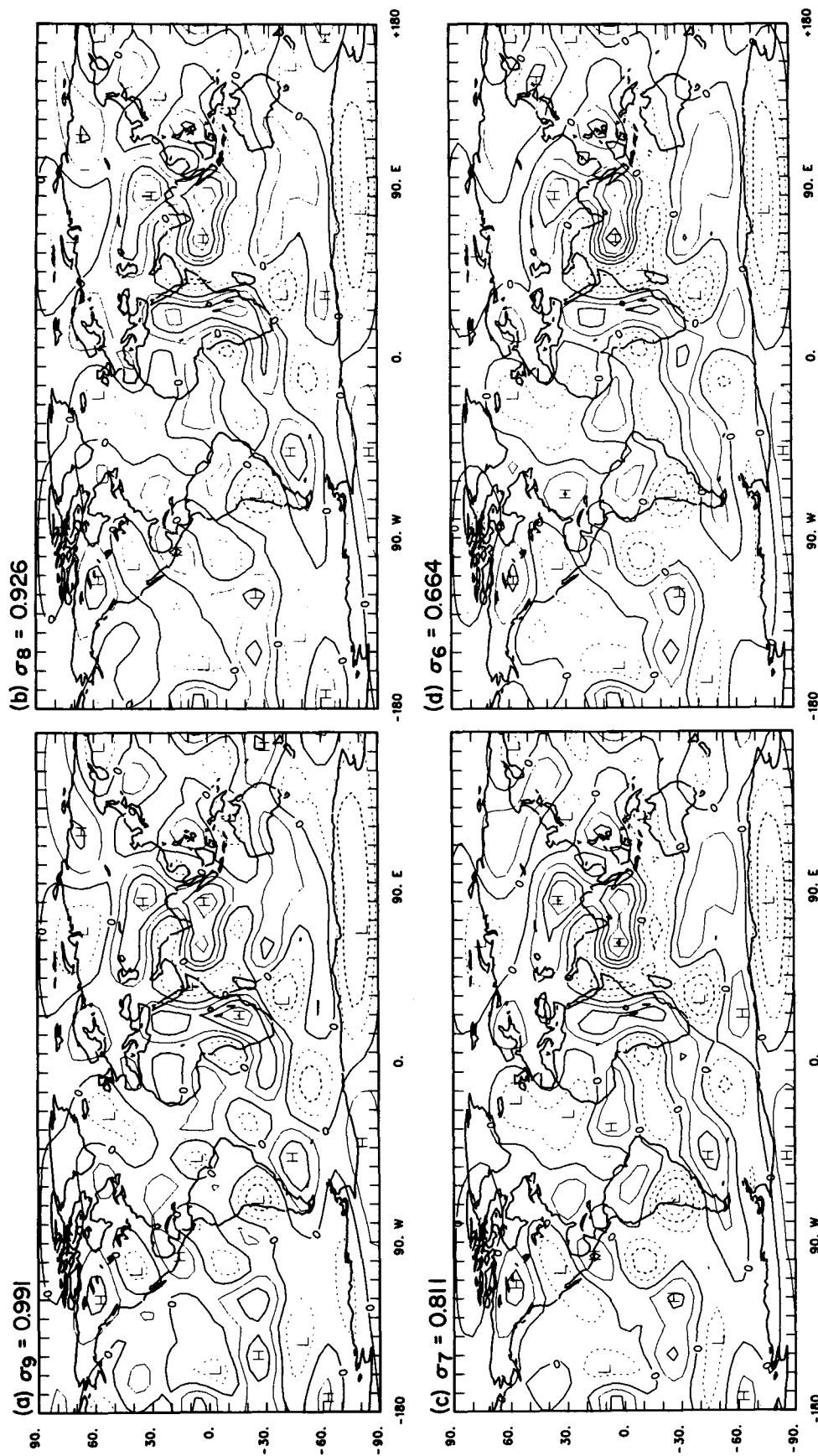
FIG. 4. As in Fig. 1, except for the SOP-II study period.

(f) $\sigma_4 = 0.366$

(e) $\sigma_5 = 0.500$

(g) $\sigma_3 = 0.189$
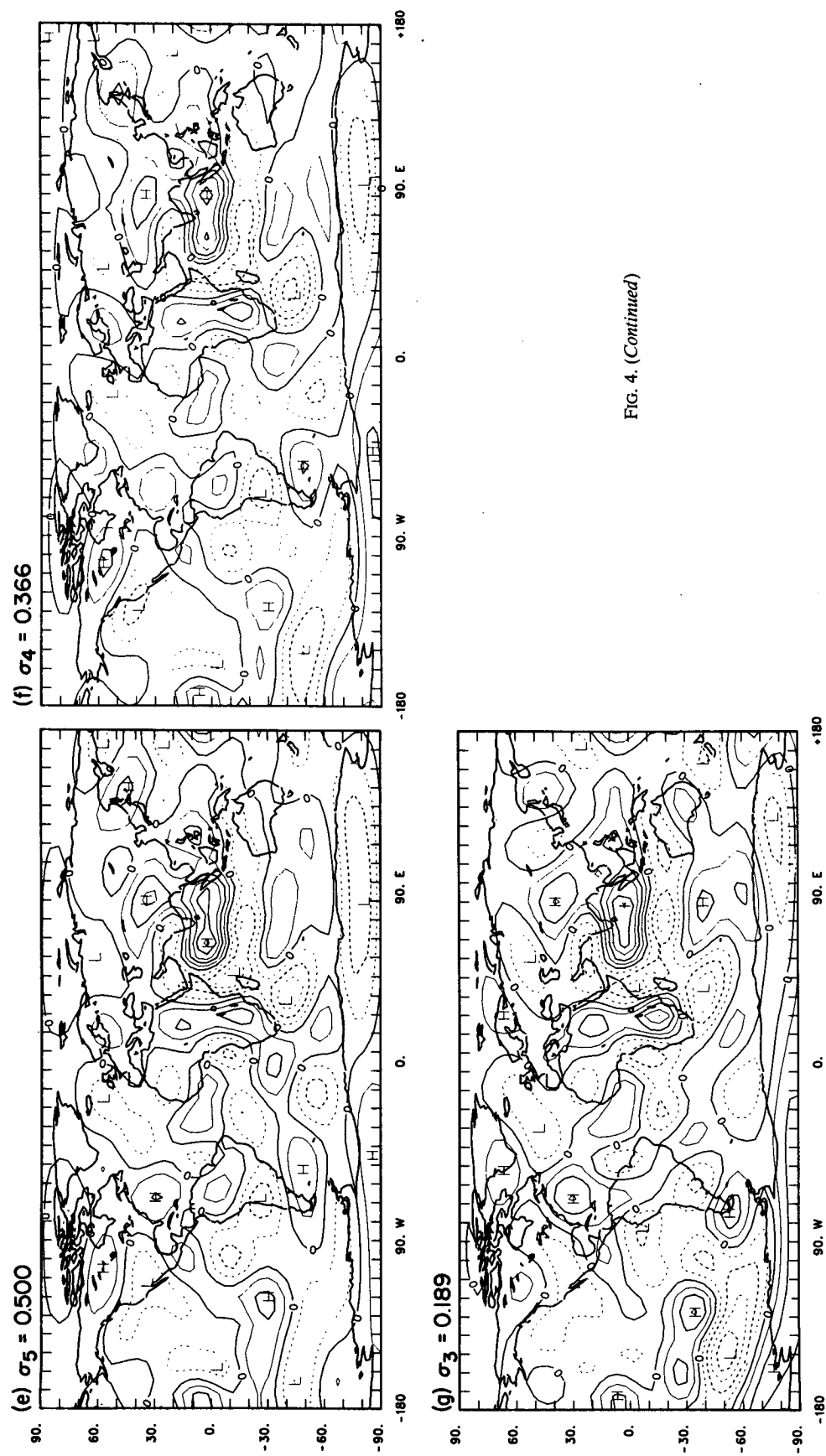
FIG. 4. (Continued)
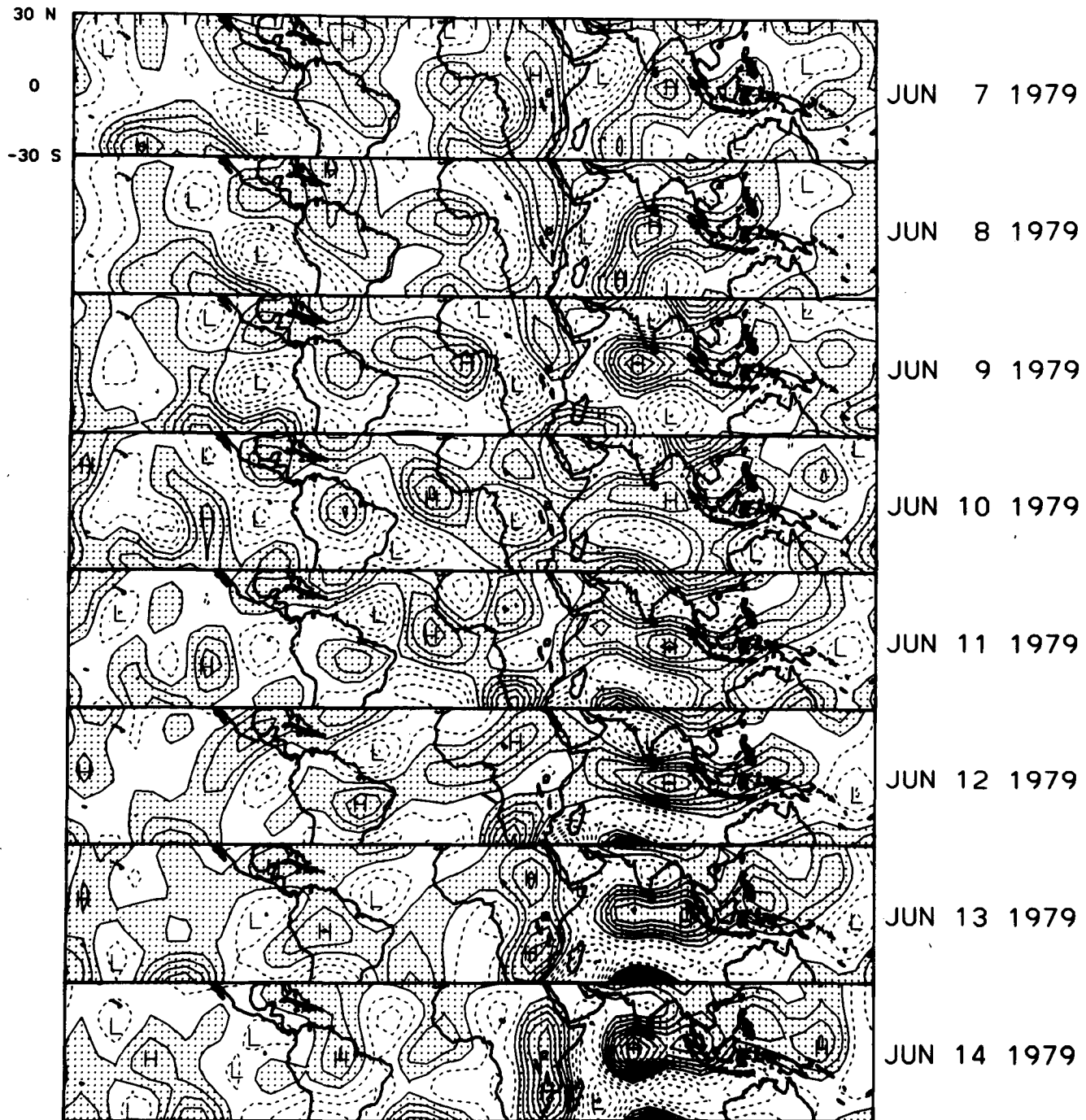
FIG. 5. As in Fig. 3, except for the SOP-II study period.

are realistic. We have mentioned in connection with Fig. 2b that there is the problem of erroneous heating over southern Africa. This problem seems to appear around 11 June and persist for the rest of the period. We know little about the cause of this problem other than the observation that the development of heating over southern Africa appears in tandem with the intensification of heating over the Indian Ocean. Our

speculation is that the objective analysis of wind over southern Africa produces an erroneous irrotational field. Earlier, Kasahara and Mizzi (1984) found unusually large temporal variations in the velocity potential over the south Indian Ocean during the SOP-II study period. They attributed this variation to errors in the analysis of the wind field. Hollingsworth et al. (1986) reported that there were systematic observa-

JUN 15 1979

JUN 16 1979

JUN 17 1979

JUN 18 1979

JUN 19 1979

JUN 20 1979

JUN 21 1979
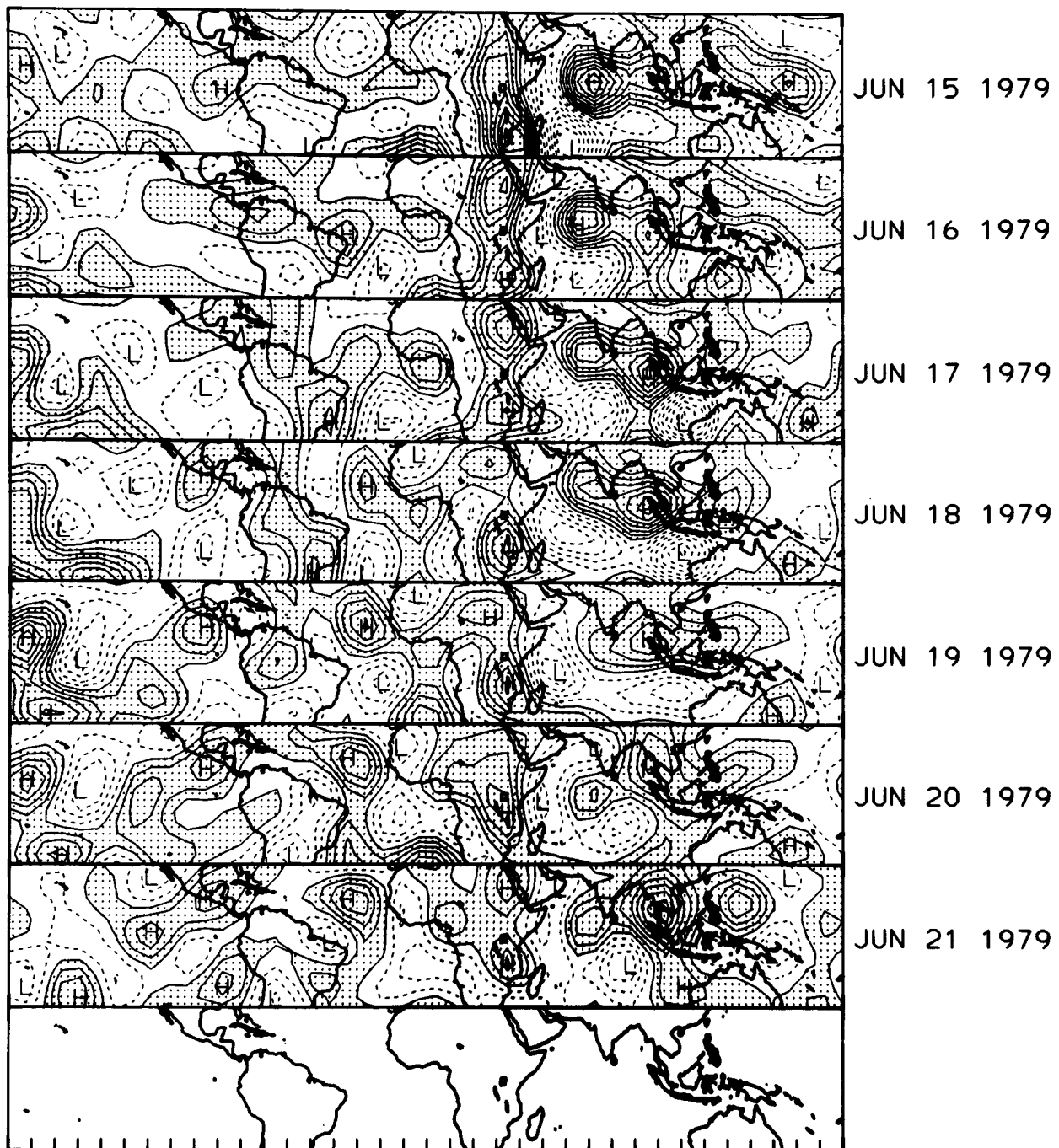
FIG. 5. (Continued)

tional errors in the upper air wind measurements at 45°S, 38°E.

5. Comparison of heating patterns with satellite imagery data

In the previous section, we briefly compared our diagnosed heating rate distributions with radiation im-

agery data from satellite measurements. In this section, we present a more quantitative comparison to provide a measure of reliability for our results. Visible and/or infrared imagery data from geostationary and polar-orbiting satellites have been used by many investigators to estimate rainfall rates in the tropics (e.g., Griffith et al., 1978; Stout et al., 1979; Richards and Arkin, 1981). These are based on the idea that deep convective clouds
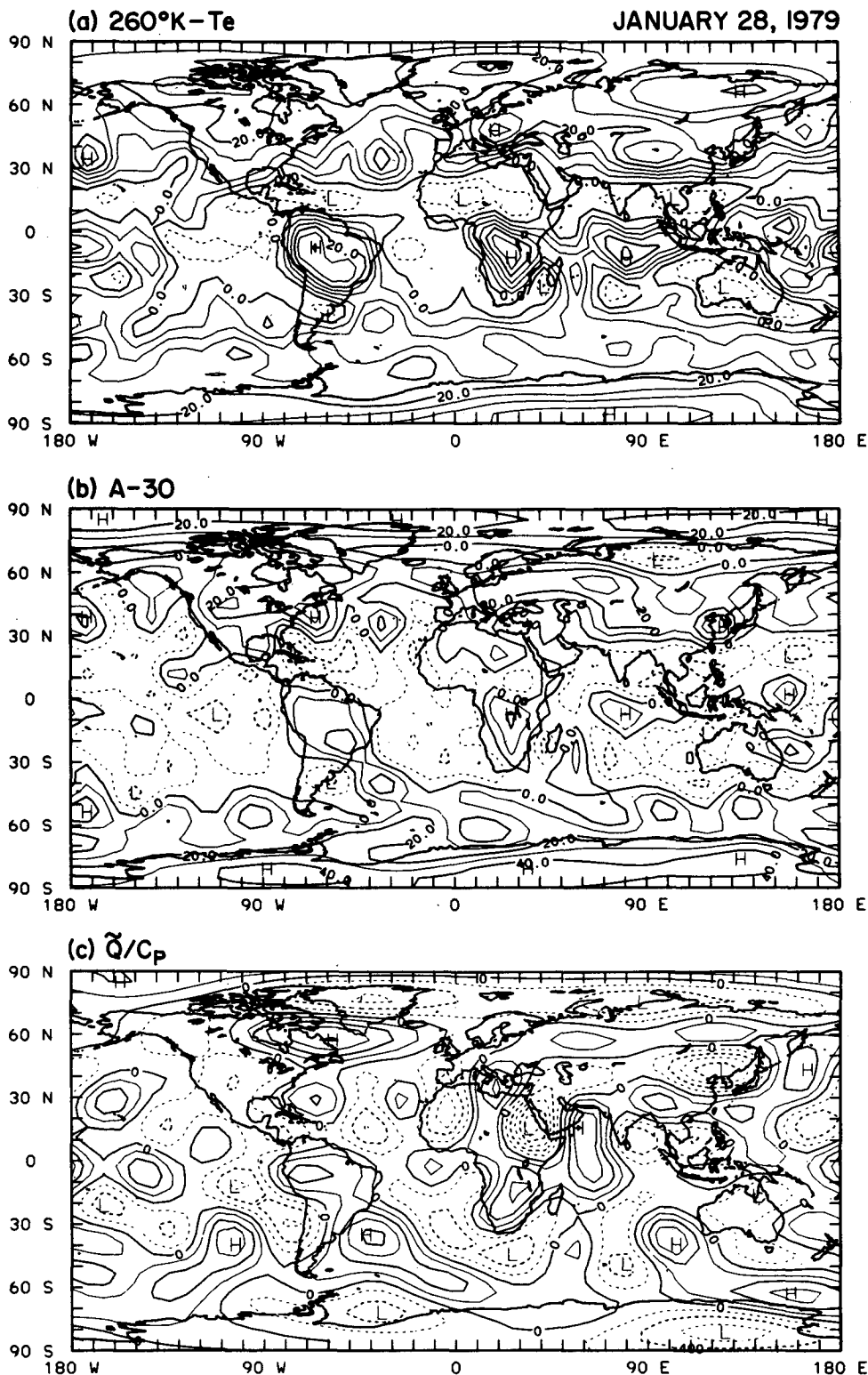
FIG. 6. (a) Pattern of 260 K $- T_e$, where T_e is IR temperature in K for 28 January 1979. Contour interval is 5 K. Positive (negative) areas delineated by solid (dashed) lines are those colder (warmer) than 260 K. (b) Pattern of albedo minus 30% for the same date. Positive (negative) areas delineated by solid (dashed) lines show those brighter (dimmer) than the global average albedo. Contour interval is 10%. (c) Pattern of mass-weighted vertically averaged diabatic heating rate $\tilde{Q}/C_p$ for the same date. Contour interval is 2×10^{-5} K s^{-1}. Dashed lines show cooling.
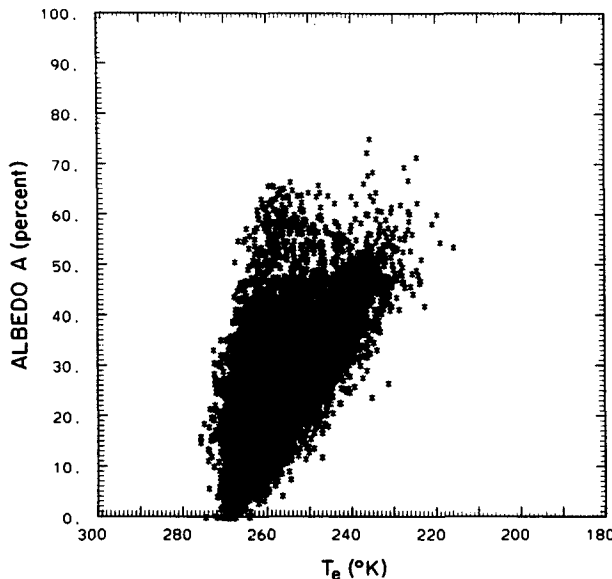
FIG. 7. Scatter diagram showing IR temperature T_e on the abscissa and albedo A on the ordinate at grid points in the 30°N–30°S zone during the SOP-I study period except for 3, 7 and 10 February 1979.

having higher tops (low temperatures) may produce more rain and on findings that the regions of rainfall tend to be correlated with bright (visible) and cold (infrared) clouds. Since tropical diabatic heating is dominated by condensation heating in deep convection, it appears useful to compare the diagnosed heating distributions with radiometric imagery data from satellites.

In this study, we use daytime infrared radiation (IR), nighttime IR, incoming solar radiation (SR) and absorbed SR data on 2.5° longitude–latitude grids processed from measurements taken by the polar-orbiting TIROS-N satellite (Gruber and Kruger, 1984). The infrared data F, given in units of W m^{-2}, are converted to equivalent blackbody temperature T_e using $F = \sigma T_e^4$, where $\sigma = 5.6693 \times 10^{-8}$ W m^{-2} K^{-4}.

A time series of the daytime and nighttime T_e plotted on a 2.5° longitude–latitude grid shows the presence of small-scale temporal variations as well as large-scale quasi-stationary features. In order to eliminate small-scale, day and night variations, we averaged the daytime and nighttime data to obtain a mean distribution for a particular day. Since we intend to compare the imagery data with our diagnosed heating rates which are smoothed with a spherical harmonics triangular 13 truncation, some degree of smoothing should be applied to the imagery data. We felt that a triangular spherical harmonic truncation retaining zonal wavenumber 0 to 18 (T18) is appropriate for the imagery data. We chose this truncation since it appears to retain most of the large-scale features while removing some of the smaller scale irregularities. Note that comparisons of diabatic heating patterns with satellite imagery data are valid only in the lower latitudes, since sources

other than convective heating are considered also important outside the tropics. In addition to the IR temperatures, we calculate albedo A from the incoming and absorbed SR data. The albedos were also smoothed with a T18 truncation.

a. SOP-I study period

First, let us examine the relationships between the distributions of IR temperature, albedo and diabatic heating rates on a daily basis. As an example, Fig. 6a shows the distribution of 260 K—T_e for a typical day during the SOP-I study period, 28 January 1979. The positive (negative) areas delineated by solid (dashed) lines are those colder (warmer) than 260 K. A constant of 260 K is chosen as an approximate value of the equivalent emission temperature for the earth–atmosphere system (Goody, 1964). Figure 6b shows the pattern of albedo minus 30%. A value of 30% is a global average albedo. The positive (negative) areas delineated by solid (dashed) lines show those brighter (dimmer) than the average albedo. Figure 6c shows the mass-weighted vertically averaged diabatic heating $\dot{Q}/C_p$ with contour intervals of 2×10^{-5} K s^{-1}. By comparing Figs. 6a and 6b in the tropics, we generally see high albedos over low IR areas such as over South America, southern Africa, the Indian Ocean, and the western central Pacific. An exception is found over the Sahara desert where both T_e and albedo are relatively high. Another exception is found over the central Pacific convergence zone where both T_e and albedo are low, suggesting the presence of cirrus clouds mixed with sparse cumulonimbus clouds.
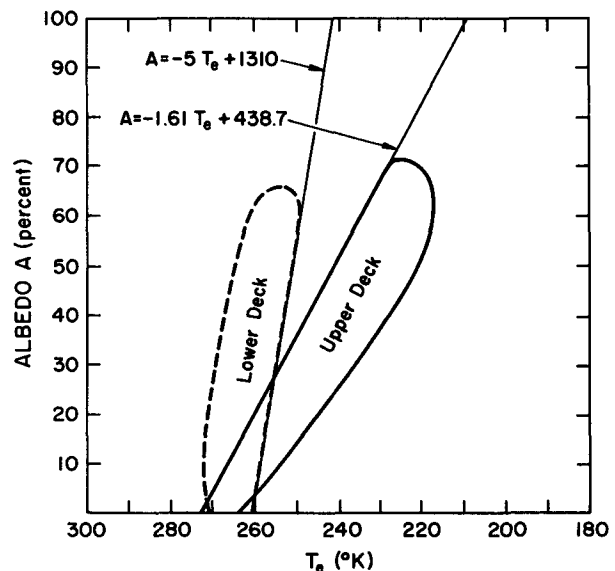

FIG. 8. Schematic diagram for Fig. 7, showing the two groups, lower deck and upper deck, of points divided by the two straight lines $A = -5.0T_e + 1310.$ and $A = -1.61T_e + 438.7$, respectively.
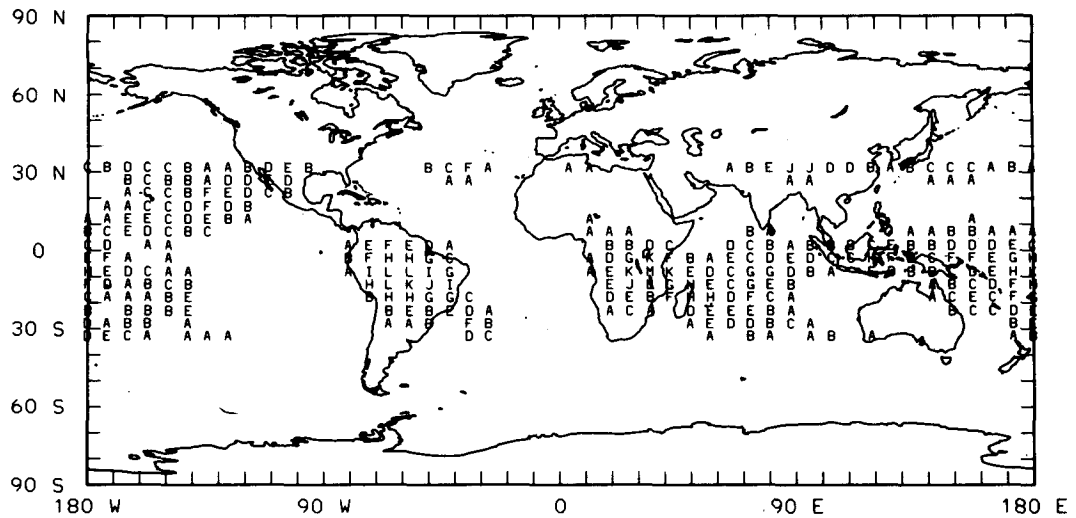
FIG. 9. Geographical map showing the locations and the number of occurrences of the plots in the upper deck shown in Fig. 7, in which albedos A are greater than 30%. The number of occurrences at each point is coded using the alphabet, $A = 1$, $B = 2$, $C = 3$, and so on.
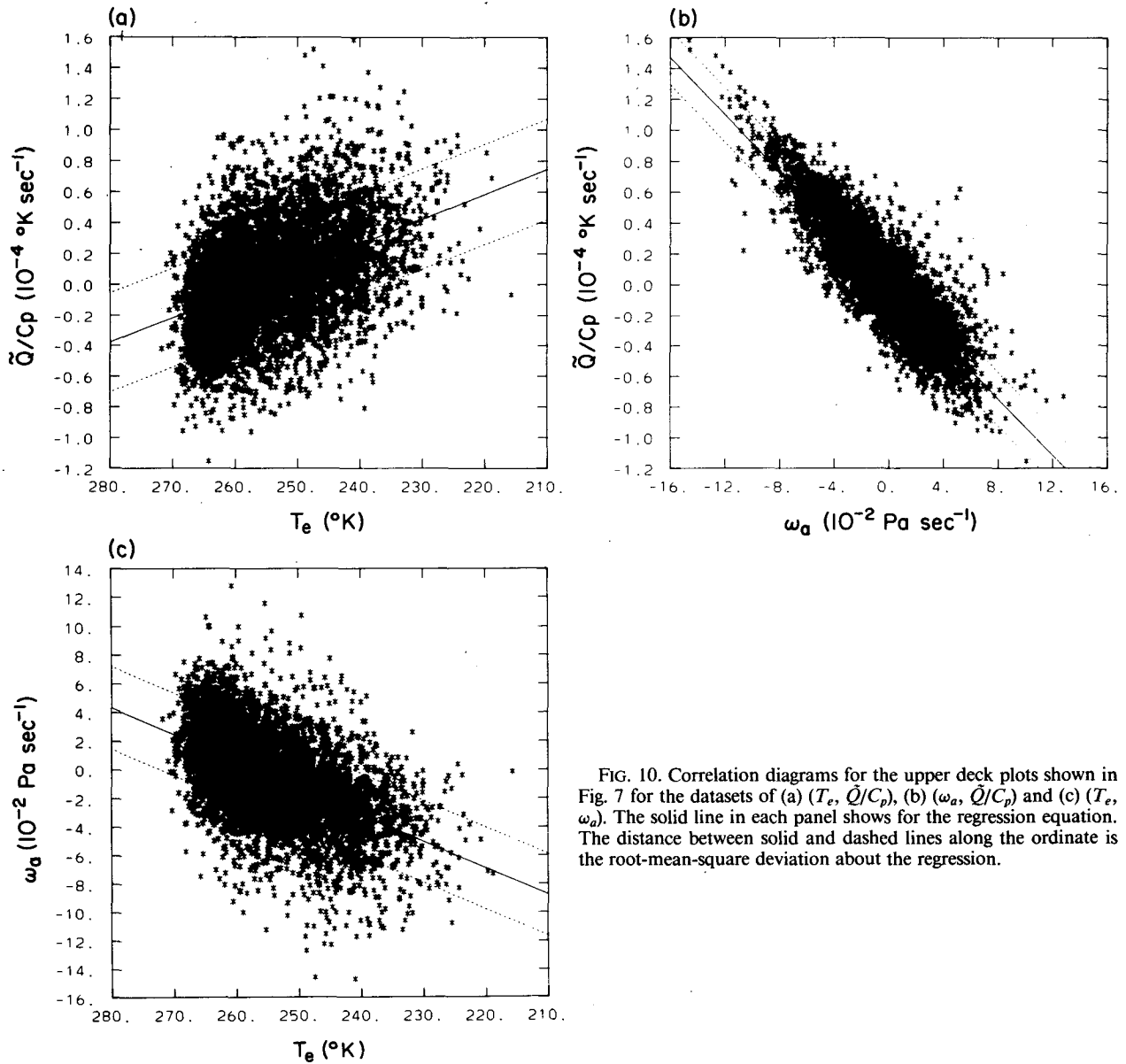

FIG. 10. Correlation diagrams for the upper deck plots shown in Fig. 7 for the datasets of (a) $(T_e, \tilde{Q}/C_p)$, (b) $(\omega_a, \tilde{Q}/C_p)$ and (c) (T_e, ω_a). The solid line in each panel shows for the regression equation. The distance between solid and dashed lines along the ordinate is the root-mean-square deviation about the regression.

TABLE 2. Values of constants α_a, β_a, . . . appearing in (5.1)–(5.3) for three different cases.

Constants	Units	Upper deck SOP-I	Lower deck $A > 50\%$ SOP-I	Upper deck SOP-II
α_a	K s^{-1}	4.1129×10^{-4}	11.566×10^{-4}	4.2235×10^{-4}
β_a	s^{-1}	-0.01603×10^{-4}	-0.04496×10^{-4}	-0.01635×10^{-4}
α_b	K s^{-1}	-0.7727×10^{-6}	0.3566×10^{-6}	0.1145×10^{-6}
β_b	K Pa^{-1}	-0.09234×10^{-2}	-0.08481×10^{-2}	-0.10316×10^{-2}
α_c	Pa s^{-1}	-48.086×10^{-2}	-117.63×10^{-2}	-44.612×10^{-2}
β_c	Pa s^{-1} K^{-1}	0.18727×10^{-2}	0.45737×10^{-2}	0.17296×10^{-2}

Figures 6a–c show a comparison of the diabatic heating distribution with the satellite imagery data. The strong heating area on Fig. 6c over South America which extends southeastward and another strong heating area over southern Africa are well correlated with the low IR temperatures and high albedos seen on Figs. 6a and 6b. Similarly, intense heating over the central Pacific corresponds to a low IR temperature and high albedo area. However, intense heating over the Indian Ocean appears to be shifted about 20° westward when compared with the location of the cold and bright cloud area over the Indian Ocean. We also see other areas of intense heating which do not match the satellite data. One such example is seen over central Africa extending westward off its west coast. There are areas of heating near or outside of 30°N–30°S which are not well correlated with the satellite data. For example, three areas of heating centered at (35°S, 105°W), (35°S, 40°W), and (35°S, 100°E) are associated with synoptic-scale midlatitude cyclones in the Southern Hemisphere. While the cyclone off the east coast of South America, centered at 35°S, 40°W is associated with low IR temperatures and high albedos, heating rates in the other two cyclones do not show a clear association with the satellite data. This finding may suggest that the surface flux of sensible heat is the principal heat source for the two cyclones. In fact, in the vertical distribution of heating rates for this particular day (not shown) we find strong heating in the lower troposphere for these two systems.

One method of identifying cloud categories from radiance measurements is with two-dimensional bispectral histograms (Platt, 1983). We constructed scatter diagrams by plotting IR temperatures T_e on the abscissa and the corresponding albedos A in percent on the ordinate. In Fig. 7 we present such a scatter diagram for data from the tropical belt (30°N–30°S) during the SOP-I study period. (3, 7 and 10 February 1979 were excluded from this analysis since the satellite data were incomplete.) Upon examining this type of histogram one can generally identify clusters of points which belong to high and low cloud categories as discussed by Platt (1983). On Fig. 7 we draw the boundaries to two clusters which are shown schematically in Fig. 8. The group of points to the right of line $A = -1.61T_e + 438.7$ is characterized by lower IR temperatures and stronger albedo dependence. We refer to this group as the "upper deck." The group of points to the left of line $A = -5.0T_e + 1310$, which is referred to as the "lower deck," contains points with higher IR temperatures and weaker albedo dependence relative to the upper deck. The boundaries for the upper and lower decks were chosen to keep the same slopes of the bispectral curves, approximated by straight lines, of albedo vs IR temperature for the idealized high and low layers shown by Platt (1983).

In the following discussion we compare the vertically averaged heating rates and the IR temperatures for two cloud categories. It is reasonable to assume that points in the upper deck are associated with cloud tops in

TABLE 3. Correlation coefficients of the datasets $(T_e, \dot{Q}/C_p)$, $(\omega_a, \dot{Q}/C_p)$, (T_e, ω_a) and (A, T_e) for various experiments in the SOP-I study period.

| Exp.	Description	Datasets			
		$(T_e, \dot{Q}/C_p)$	$(\omega_a, \dot{Q}/C_p)$	(T_e, ω_a)	(A, T_e)
1	All points	-0.36	-0.86	0.45	-0.66
2	Lower deck	-0.20	-0.84	0.21	-0.54
3	Upper deck	-0.42	-0.87	0.52	-0.94
4	Lower deck $A > 40\%$	-0.27	-0.82	0.35	-0.30
5	Lower deck $A > 50\%$	-0.46	-0.86	0.46	-0.21
6	Lower deck $A < 30\%$	-0.18	-0.84	0.17	-0.47
7	Upper deck $A > 40\%$	-0.22	-0.89	0.23	-0.61
8	Upper deck $A > 50\%$	-0.24	-0.88	0.19	-0.50
9	Upper deck $T_e < 257$ K	-0.28	-0.87	0.36	-0.86
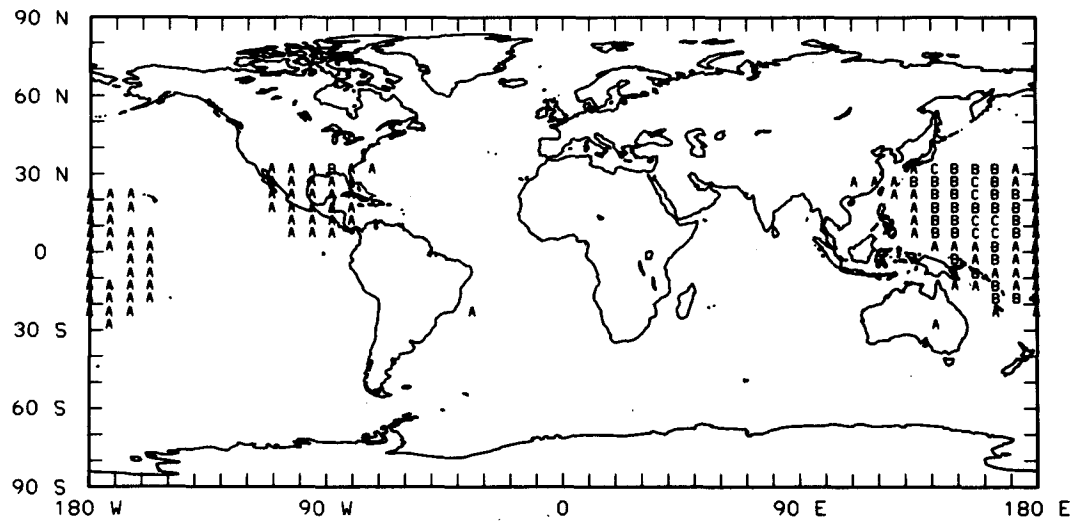
FIG. 11. As in Fig. 9, except for the lower deck in which albedos A are greater than 50%.

(a)

(b)

(c)
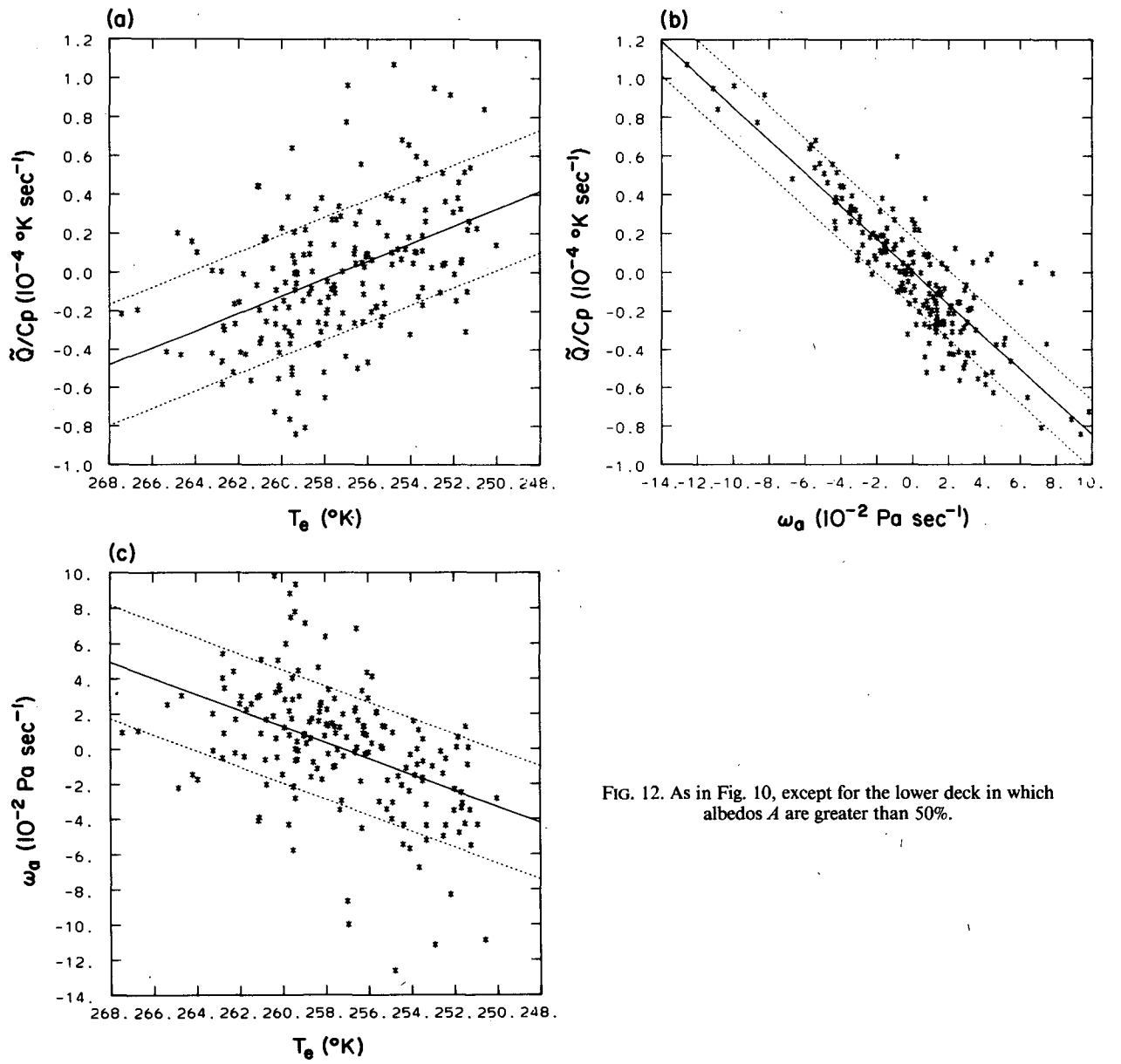
FIG. 12. As in Fig. 10, except for the lower deck in which albedos A are greater than 50%.

(a) 260°K – Te   JUNE 22, 1979

(b) A – 30

(c) $\tilde{Q}/C_P$
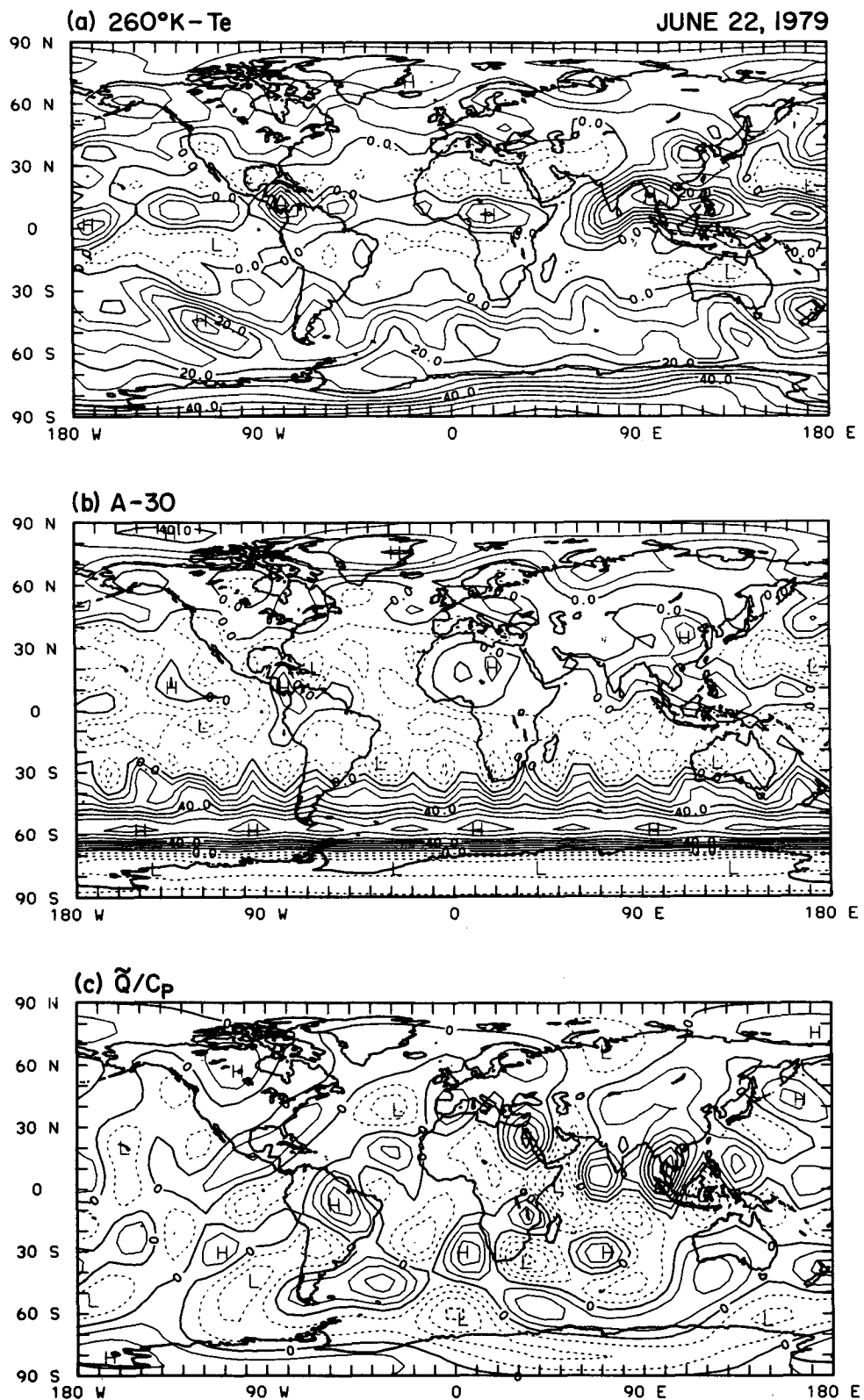
FIG. 13. As in Fig. 6, except for 22 June 1979, during the SOP-II study period.
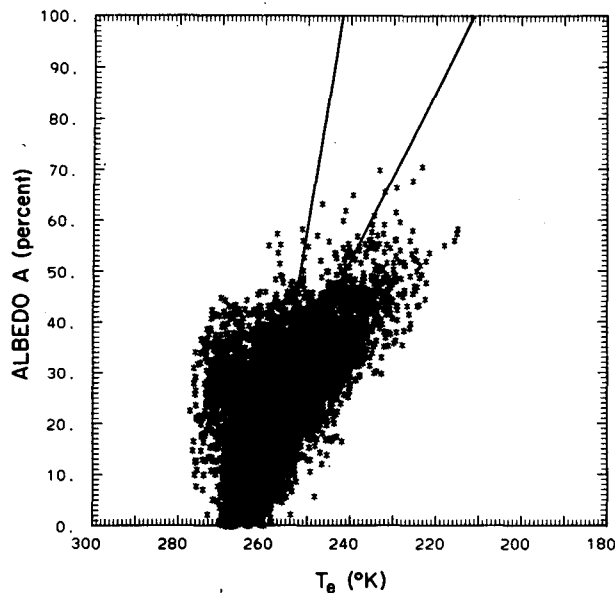
FIG. 14. As in Fig. 7, except for the SOP-II study period, excluding 15, 16, and 17 June 1979. The two solid lines are identical to those shown in Fig. 8 to separate the points into the upper and lower decks.

regions of deep cumulus convection, while points in the lower deck are associated with cloud tops in regions of shallow convection. By choosing an appropriate temperature and/or albedo cutoff, we may isolate points in the upper and lower decks which have similar synoptic conditions. As an example, we show in Fig. 9 the locations and the number of occurrences where the albedos exceed 30% for the upper deck. Note that the highest frequencies are in regions of deep convection. Since tropical diabatic heating is dominated by convective heating, we expect good correlations between diabatic heating and IR temperature in the upper deck.

Figure 10a shows the correlation diagram for IR temperature T_e on the abscissa and vertically averaged heating rate $\tilde{Q}/C_p$ in units of 10^{-4} K s^{-1} on the ordinate for all points in the upper deck. Figure 10b shows the correlation diagram for $\tilde{Q}/C_p$ and the lower tropospheric average vertical p-velocity ω_a (units of 10^{-2} Pa s^{-1}) below the $\sigma = 0.5$ level. A unit scale 10 means 10 $\times 10^{-2}$ Pa s^{-1} and is equivalent to 0.001 mb s$^{-1} \approx 86.4$ mb day^{-1}. Similarly, Fig. 10c shows the correlation diagram for ω_a and T_e. The solid line in each figure is the regression line, and the distance between the dashed lines and the solid line along the ordinate is the root-mean-square deviation about the regression. The equations for the regression lines shown in Figs. 10a–c are as follows:

$$\tilde{Q}/C_p(\text{K s}^{-1}) = \alpha_a + \beta_a T_e(\text{K}) \qquad (5.1)$$

$$\tilde{Q}/C_p(\text{K s}^{-1}) = \alpha_b + \beta_b \omega_a(\text{Pa s}^{-1}) \qquad (5.2)$$

$$\omega_a(\text{Pa s}^{-1}) = \alpha_c + \beta_c T_e(\text{K}). \qquad (5.3)$$

Numerical values of the constants $\alpha_a, \beta_a, \ldots$ are listed under "Upper deck, SOP-I" in Table 2 together with those of other cases to be discussed later.

One notable observation in Fig. 10a–c is that the threshold temperature T_e^* which satisfies the condition of $\tilde{Q} = 0$ in (5.1) and divides the positive and negative heating rates is 256.6 K. Similarly, the threshold T_e^* which satisfies the condition of $\omega_a = 0$ in (5.3) is 256.7 K.

Table 3 shows the correlation coefficients (CC) of the datasets $(T_e, \tilde{Q}/C_p)$, $(\omega_a, \tilde{Q}/C_p)$, (T_e, ω_a) and (A, T_e) for various experiments. The case presented in Figs. 10a–c, all points in the upper deck, is listed as Exp. 3. In this experiment, the correlation coefficient (CC) of $(T_e, \tilde{Q}/C_p)$ is -0.42, indicating that the lower the temperature T_e, the higher the heating rate. The large value, -0.87 of the CC for $(\omega_a, \tilde{Q}/C_p)$ is a reflection of the fact that $\tilde{Q}/C_p$ and ω_a are highly interdependent in the
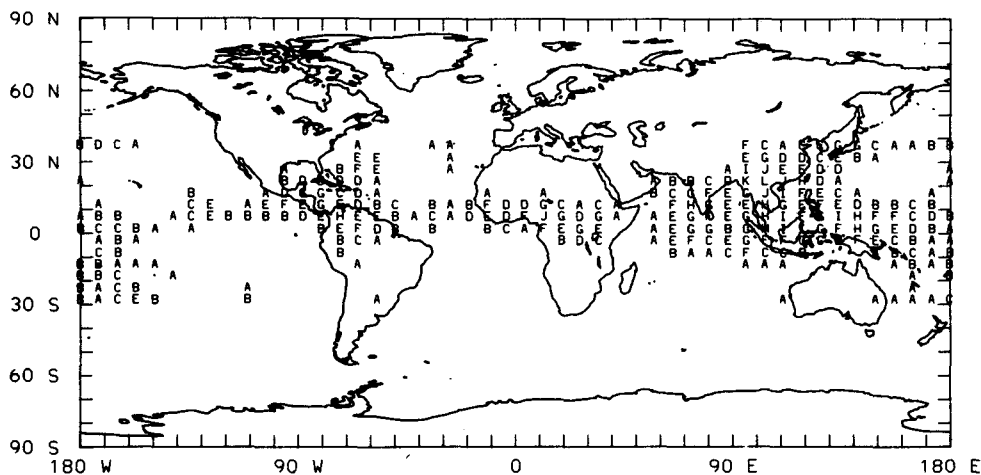

FIG. 15. As in Fig. 9, except for the upper deck plots shown in Fig. 14 in which albedos A exceed 30%.

(a)

(b)

(c)
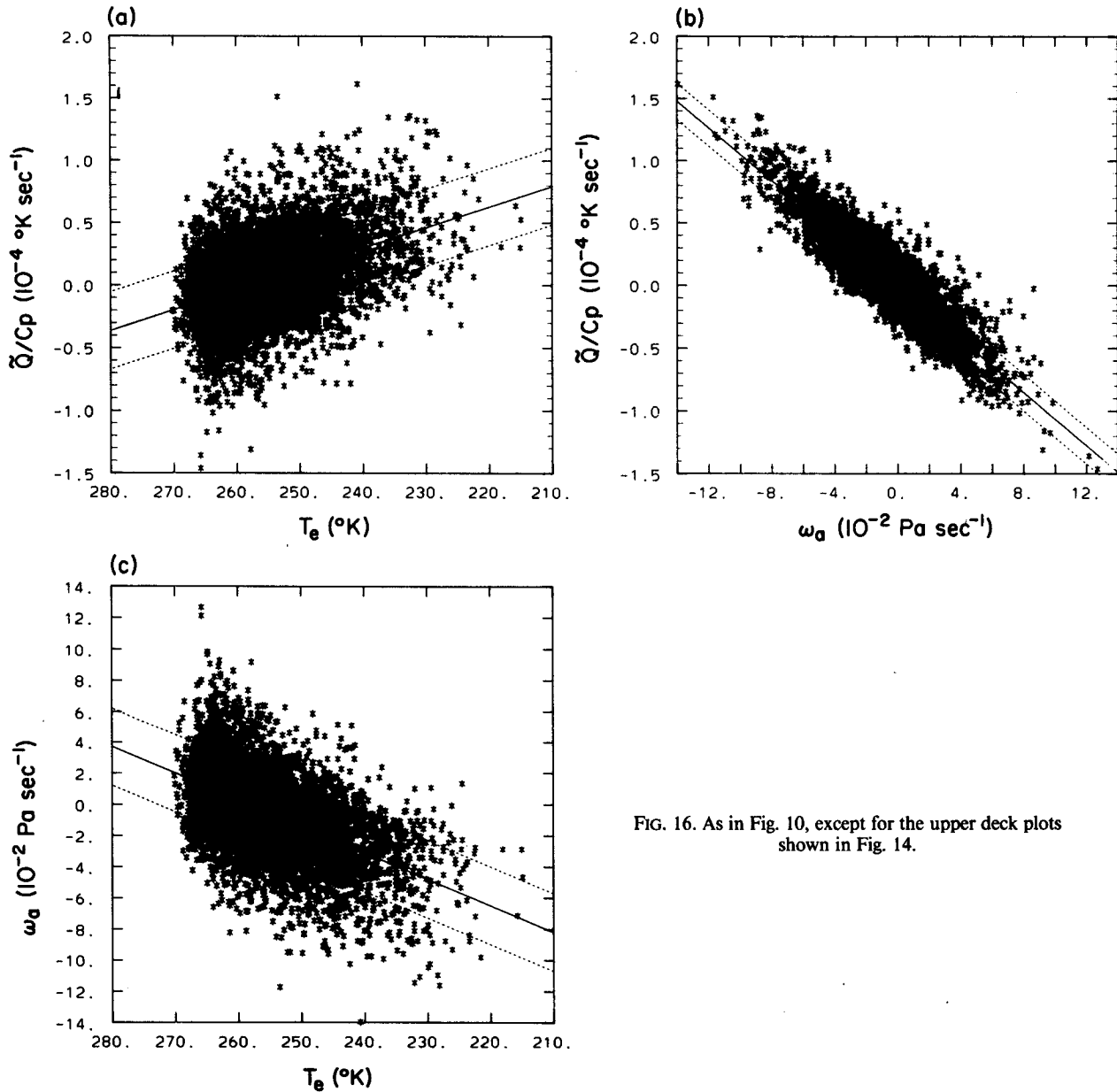
FIG. 16. As in Fig. 10, except for the upper deck plots shown in Fig. 14.

tropics as can be shown by scale analysis (Kasahara, 1982). The CC of (T_e, ω_a) is 0.52 indicating that the lower the IR temperature T_e, the stronger the upward motion. A high CC, -0.94 for (A, T_e) is a reflection of selecting this particular group.

In Table 3, Exp. 1 includes all points in the region between 30°N–30°S. Experiment 2 examines points in the lower deck. Comparison of the CCs for Exps. 1–3 shows that the data stratification improves the relationship between T_e and $\tilde{Q}/C_p$ or ω_a. In order to understand some features of the lower deck, Exps. 4 to 6 were conducted to see which portion of the lower deck yields good correlations of, e.g., $(T_e, \tilde{Q}/C_p)$. Experiment 4 involves points in the lower deck with the additional

condition that $A > 40\%$, while Exp. 5 is the same, except for $A > 50\%$. It is of interest to find that Exp. 5 gave a good CC of -0.46 for $(T_e, \tilde{Q}/C_p)$, indicating that warm and dim points (e.g., over oceans) are not useful for inferring $\tilde{Q}/C_p$ from T_e.

Figure 11 is the same as Fig. 9, except for points in the lower deck with $A > 50\%$ (Exp. 5). After examining the synoptic conditions at these locations, we found that they are generally associated with outbreaks of cold air from the North American continent and from the Asiatic continent during the winter monsoon. Consequently, the source of heating is likely to be the transport of sensible and latent heat from the oceans.

Figures 12a–c show correlation diagrams similar to

those of Figs. 10a–c, except for Exp. 5. The regression constants for this case are shown in Table 2 under "Lower deck, $A > 50\%$, SOP-I." The threshold values of T_e^* corresponding to $\tilde{Q} = 0$ in (5.1) and $\omega_a = 0$ in (5.3) are 257.3 and 257.2 K, respectively. These values agree closely with those of the upper deck, indicating that the threshold temperatures do not depend very much on the stratification of data points used.

Experiments 7–9 of Table 3 are designed to test data stratification for the correlations of $(T_e, \tilde{Q}/C_p)$ and (T_e, ω_a) in the upper deck. Experiments 7 and 8 deal with the portions of the upper deck where $A > 40\%$ and 50%, respectively. Experiment 9 is concerned with points in the upper deck where $T_e < 257$ K. Since $T_e = 257$ K is approximately the threshold temperature T_e^*, Exp. 9 selects data points in areas of lower tropospheric ascending motion. The finding that the CCs of $(T_e, \tilde{Q}/C_p)$ and (T_e, ω_a) in Exp. 3 are still higher than those of Exp. 9 suggests that the IR temperature pattern can be used to infer both ascending and descending motion. Comparison of Exps. 7 and 8 with Exp. 3 indicates that the strength of the correlation comes from all upper deck points in contrast to the lower deck case in which the best correlations are found in points with high albedo and low IR temperature.

b. SOP-II study period

Now, let us examine a typical day during the SOP-II study period. Figures 13a–c are the same as Figs. 6a–c, except for 22 June 1979. We see that intense heating over the Southeast Asian monsoon region agrees very well with the area of high albedos and low IR temperatures. However, the rest of the heating in the 30°N–30°S zone does not appear to be well correlated with the imagery data. For example, cold IR temperatures (Fig. 13a) are found around the globe near 10°N. Although the strong convection seems to be more locally concentrated as seen from the albedo pattern (Fig. 13b), the pattern of heating and cooling (Fig. 13c) in the tropics of the western hemisphere is oriented in a northeast–southwest direction in contrast to the zonal configuration of the IR temperature pattern.

Figure 14 shows a scatter diagram, the same as Fig. 7 except for the SOP-II study period. (15, 16 and 17 June are excluded since the satellite imagery data are incomplete.) The two straight lines on Fig. 14 are the same as those in Fig. 8, dividing the points into upper and lower decks.

Figure 15 is the same as Fig. 9, except for upper deck points with $A > 30\%$ during the SOP-II study period. These locations appear to coincide with those of deep moist convection.

Figures 16a–c show correlation diagrams for $(T_e, \tilde{Q}/C_p)$, $(\omega_a, \tilde{Q}/C_p)$ and (T_e, ω_a), respectively, for the upper deck, similar to Figs. 10a–c, except for the SOP-II study period. The constants for the regression equations (5.1)–(5.3) in this case are shown in the last column of Table 2. By comparing the regression constants in (5.1)–(5.3) for the upper deck of SOP-II with those of SOP-I, we find differences on the order of 10%, suggesting that the regression equations are insensitive to seasonality. The threshold temperatures T_e^* determined from (5.1) and (5.3) in this case are 258.3 and 258.2 K, respectively. These values are very close to those of the upper deck, SOP-I.

Table 4 lists the CC of the datasets $(T_e, \tilde{Q}/C_p)$, $(\omega_a, \tilde{Q}/C_p)$, (T_e, ω_a) and (A, T_e) for various experiments similar to those of Table 3. Experiment 1S includes all points in the region between 30°N and 30°S. Experiments 2S and 3S deal with all points of the lower and upper deck, respectively. Experiment 3S is the case shown in Figs. 16a–c. It is of interest to find that the CCs for Exp. 3S are almost identical to those of Exp. 3 in Table 3. In fact, the results of Exp. 1S and Exp. 1 are very close too. However, the results of Exp. 2S are considerably different from those of Exp. 2. This may be explained by observing that the lower deck of the SOP-II study period contains brighter $(A > 30\%)$ points with considerably higher T_e than that of the SOP-I study period. For example, high albedos are found over the Sahara (Fig. 13b) where the IR temperatures (Fig. 13a) are high. The heating rates (Fig. 13c) over the Sahara show a mixed relationship with T_e.

Experiments 4S and 5S are designed to find out whether or not additional constraints on the upper deck can increase the correlation between T_e and $\tilde{Q}$ or ω_a.

TABLE 4. Correlation coefficients of the datasets $(T_e, \tilde{Q}/C_p)$, $(\omega_a, \tilde{Q}/C_p)$, (T_e, ω_a), and (A, T_e) for various experiments in the SOP-II study period.

Exp.	Description	Datasets			
		$(T_e, \tilde{Q}/C_p)$	$(\omega_a, \tilde{Q}/C_p)$	(T_e, ω_a)	(A, T_e)
1S	All points	−0.35	−0.88	0.44	−0.66
2S	Lower deck	−0.01	−0.84	0.05	−0.34
3S	Upper deck	−0.41	−0.89	0.50	−0.92
4S	Upper deck $A > 20\%$	−0.37	−0.91	0.42	−0.84
5S	Upper deck $T_e < 257$ K	−0.36	−0.91	0.41	−0.82
6S	All points 40°N–20°S	−0.36	−0.88	0.47	−0.67
7S	Lower deck 40°N–20°S	−0.01	−0.85	0.09	−0.29
8S	Upper deck 40°N–20°S	−0.45	−0.91	0.53	−0.92

The results indicate that the answer seems to be negative, as in Exps. 7 and 9 shown in Table 3.

Experiments 6S–8S are the same as Exps. 1S–3S, except the domain is shifted 10 degrees northward to 40°N–20°S. This shift improves the correlations of $(T_e, \tilde{Q}/C_p)$ and (T_e, ω_a). This improvement may be explained by the fact that the northern excursion of the intertropical convergence zone in June is greater than its southern excursion in January. Consequently, deep convection associated with the Asiatic monsoon extends higher into the midlatitudes of the Northern Hemisphere.

6. Discussion and conclusions

We evaluated the global distribution of diabatic heating with the thermodynamic energy budget and ECMWF Level IIIb FGGE analyses. We examined two 15-day periods during the FGGE SOP-I and II in 1979. Although our 15-day averages of the mass-weighted vertically averaged diabatic heating rates generally agree with the results obtained by other investigators, details such as their magnitude and even the spatial distributions are different due to many differences in the computing schemes, the analysis datasets and the analysis periods. In the Appendix, we present a preliminary comparison of the ECMWF heating rates for the SOP-I study period with the heating rates obtained from the GFDL Level IIIb data. On the one hand, it is assuring to see many agreements between the ECMWF and GFDL heating rates. On the other, we see significant differences, and feel further study is necessary to resolve the question of data reliability.

In this study, we have made an effort to examine the daily variation of tropospheric diabatic heating in contrast with other investigations which dealt with the climatological aspects. Our overall impression is that the temporal variations of large-scale heating appear to be related to the synoptic features of the global circulation, although some features of the heating, such as relatively strong heating over southern Africa during the SOP-II study period, seem to be erroneous. Thus, it is reasonable to ask, how reliable is the evaluation of the diabatic heating rates on a daily basis.

In attempting to answer the question, Mohanty et al. (1986) performed two sensitivity experiments using the NCAR Community Forecast Model and its associated nonlinear normal mode initialization package (Errico, 1983). One experiment was to test the impact of diabatic heating on the initialization of the prediction model. The other was to test its impact on 24-hour forecasts. For both experiments, the use of the diagnosed heating distributions gave beneficial effects compared with the use of model-generated heating distributions.

We have made a more direct examination of the diagnosed heating rates in the 30°N–30°S band by comparing them with the visible and infrared radiometric imagery data from the TIROS-N polar-orbiting satellite. By examining the distributions of albedo and IR temperature for both the SOP-I and II study periods, we found that there are regions of heating and upward motion which are correlated with bright (high albedo) and cold (low IR temperature) portions, referred to as the "upper deck," of the imagery data. Regression equations were obtained for the datasets $(T_e, \tilde{Q}/C_p)$, $(\omega_a, \tilde{Q}/C_p)$, and (T_e, ω_a). We found that the threshold IR temperatures which satisfy the condition of $\tilde{Q} = 0$ or $\omega_a = 0$ for the upper deck in both the SOP-I and II study periods are approximately 257 K and nearly independent of the cloud type stratification and the season. The values of $\Delta(\tilde{Q}/C_p)/\Delta T_e$, which is β_a in (5.1), for the upper deck in the SOP-I and II study periods are almost identical (see Table 2). Arkin (1984) obtained a regression relationship between rainfall rates and infrared radiation flux data from satellites. Using departures from climatological means, he converted rainfall rate anomaly to condensational heating anomaly in the tropics (20°N–20°S). He then obtained a formula between the implied diabatic heating rates and the IR flux data. The range of our heating rates agrees reasonably well with that of Arkin.

We found that for almost all cases examined here, IR temperatures T_e are better correlated with ω_a than $\tilde{Q}$. Nevertheless, the best CC value between T_e and ω_a was 0.53. It may be pertinent to comment on the CCs obtained by other investigators when comparing infrared satellite data with *observed* rainfall rates. Although the range of values quoted in the literature varies widely, the maximum values are approximately 0.8 (e.g., Griffith et al., 1978; Arkin, 1979). If we allow the hypothesis that satellite imagery data are equally correlated with vertical motions as are rainfall rates, then we can interpret the difference in the CC values of 0.5 and 0.8 as an indication of inaccuracy in the vertical motion fields used in this study. Remember that both $\tilde{Q}$ and ω_a are diagnosed quantities inferred from the analyses rather than ground truths measured directly by instruments.

It is widely recognized that the quality and quantity of current meteorological observations are not good enough to analyze accurately the irrotational part of the velocity field. Moreover, a special difficulty exists in analyzing the tropical wind field due to the complicated relationship between the mass and velocity fields (Daley, 1985). From this study, it is our impression that the judicious use of infrared radiance data can improve the analysis of the vertical motion field in the tropics. To this end, Julian (1984) proposed a scheme to provide better estimates of the mass divergence field in the tropics utilizing satellite infrared radiance data. The use of improved vertical motion should lead to more accurate determination of the global diabatic heating rates.

(b) $\sigma_8 = 0.926$

(d) $\sigma_6 = 0.664$

(a) $\sigma_9 = 0.991$

(c) $\sigma_7 = 0.811$
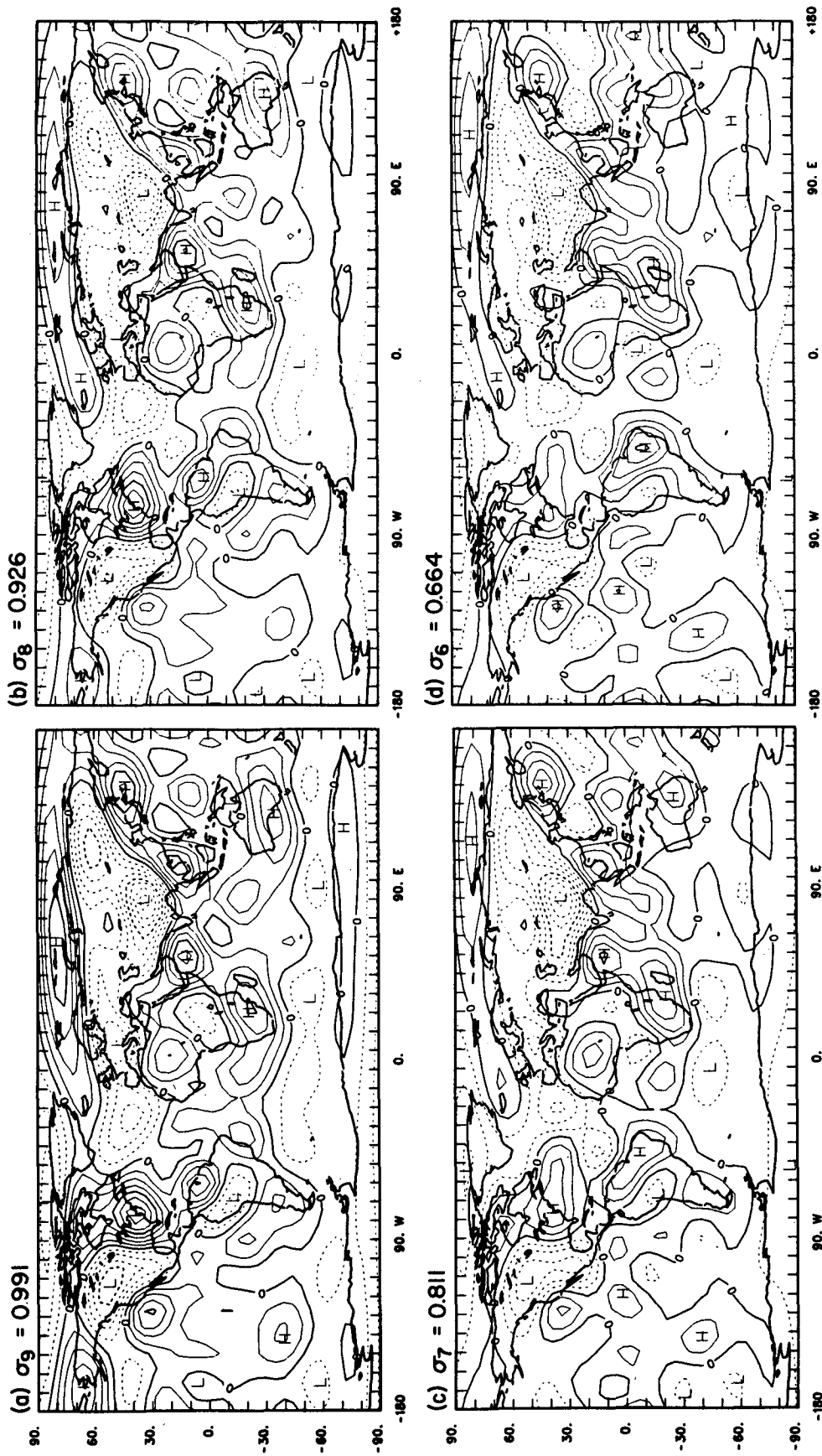
FIG. 17. As in Fig. 1, except for the GFDL Level IIIb dataset.

FIG. 17. (Continued)

APPENDIX

Global Distribution of Heating Rates for SOP-I Study Period Obtained from the GFDL FGGE Level IIIb Data

As one measure of reliability in the diabatic heating calculations, we present the results from the GFDL Level IIIb data for the SOP-I study period, 27 January to 10 February 1979. The analysis scheme of GFDL is described by Stern et al. (1985). We calculated diabatic heating rates with the same procedure as described in section 2.

Figure 17 shows the diabatic heating rates, Q_k/C_p averaged during the SOP-I study period at each σ_k level and calculated from the GFDL data. This figure should be compared with Fig. 1 obtained from the ECMWF data. Let us first discuss the comparison between Fig. 17a and Fig. 1a at the $\sigma_9 = 0.991$ level. Except for two intense heating areas, one off the east coast of North America and the other off the south coast of Australia, the ECMWF heating rates are generally weaker than the GFDL heating rates. The spatial distribution of the GFDL heating rates shows a clearer contrast between the continents and the oceans in the Northern Hemisphere than is shown by the ECMWF heating rates. Particularly, the strong heating contrast over the east coast of Asia stands out more clearly in the GFDL results. We have already pointed out in section 3 that heating over the Tibetan Plateau is an unrealistic feature of the ECMWF results. In the GFDL results, heating exists over the eastern Pacific off the California coast. This feature is absent from the ECMWF results. Elsewhere, agreement between the GFDL and ECMWF results, such as over Africa and South America, is generally quite good.

Let us next discuss the comparison between Fig. 17g and Fig. 1g at the $\sigma_3 = 0.189$ level. At this level, agreement between the GFDL and ECMWF results appears to diminish. Also, the GFDL heating rates at this level are considerably larger than the ECMWF heating rates. At σ_3 the ECMWF heating rates are of the same order as those at the lower levels, while the GFDL heating rates become noticeably different from those of the lower levels.

The vertical distribution of the GFDL heating rates seems to be as consistent as that of the ECMWF heating rates. The source of heating over the oceans off the east coasts of North America and Asia is likely to be the transport of sensible and latent heat from the oceans, since the heating rates are large in the lower troposphere and decrease upwards. In contrast, the source of heating over South America, South Africa, and the East Indies is likely to be the release of latent heat from condensation in deep moist convection, because the heating rates are relatively weak near the earth's surface, and increase upward becoming rather strong at σ_3.
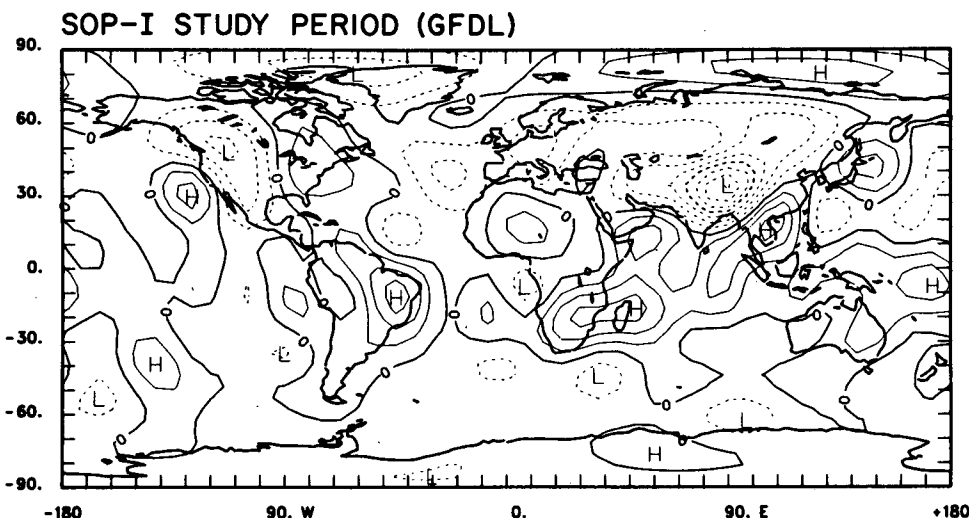

FIG. 18. As in Fig. 2a, except for the GFDL Level IIIb dataset.
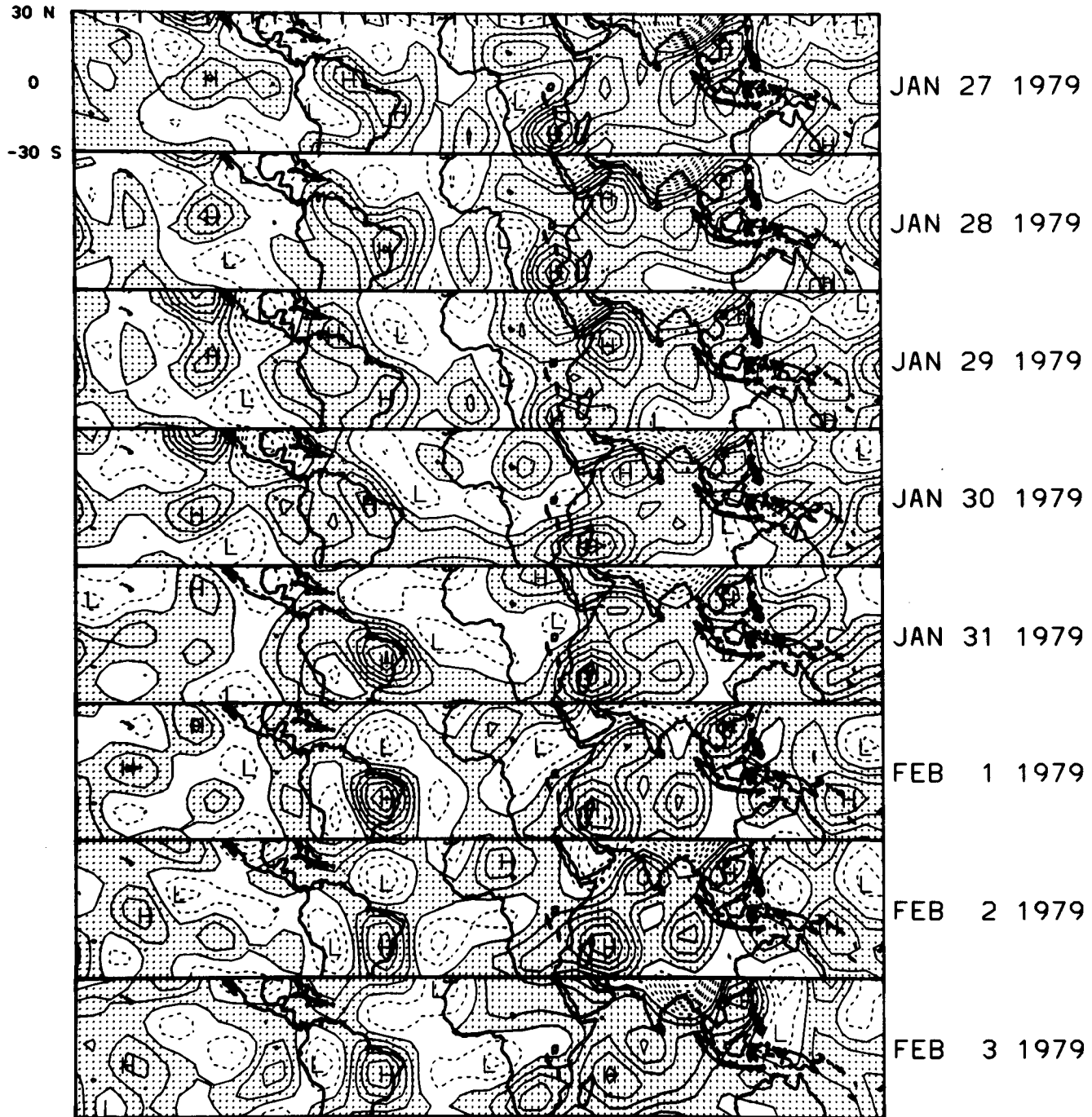
FIG. 19. As in Fig. 3, except for the GFDL Level IIIb dataset.

Figure 18 shows the 15-day average of the mass-weighted vertically averaged heating rates calculated from the GFDL data for the SOP-I study period. This figure should be compared with Fig. 2a obtained from the ECMWF data. Although the GFDL average heating rates are somewhat larger than the ECMWF average heating rates, they are about the same order of mag-nitude. Many features seen in Fig. 18 have already been discussed in conjunction with Fig. 17.

Figure 19 shows a daily series of the mass-weighted vertically averaged heating rates between 30°N and 30°S during the SOP-I period based on the GFDL data. This figure should be compared with Fig. 3 obtained from the ECMWF data. Heating areas are stippled. By

FEB 4 1979

FEB 5 1979

FEB 6 1979

FEB 7 1979

FEB 8 1979

FEB 9 1979

FEB 10 1979
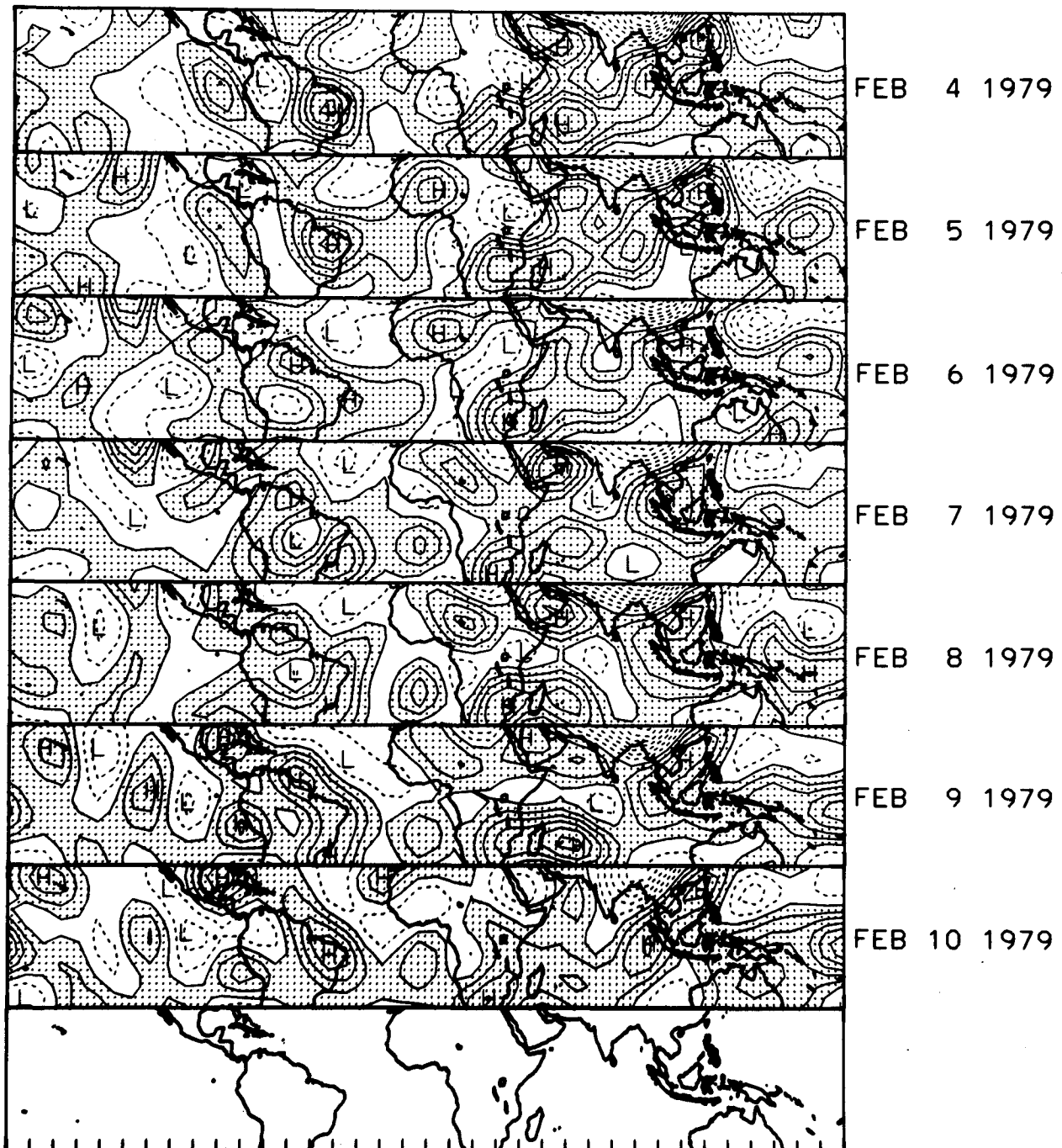
FIG. 19. (*Continued*)

examining the temporal development of the synoptic features in Figs. 3 and 19, we find both areas of agreement and disagreement. For example, we discussed the time variation of heating over South America in section 3. The movement of a heating maximum over the Amazon Basin between 28–29 January and 1–2 February in Fig. 3 is seen on Fig. 19 as well. The fact that

this is a credible synoptic feature may be seen from Fig. 20, which shows a time series of the daily IR temperature T_e (smoothed with a T18 truncation) obtained from the TIROS-N in the tropics between 30°N and 30°S. As discussed in section 5, the areas colder than 258 K are considered to be those of heating and are stippled. Although the daily progression of heating over
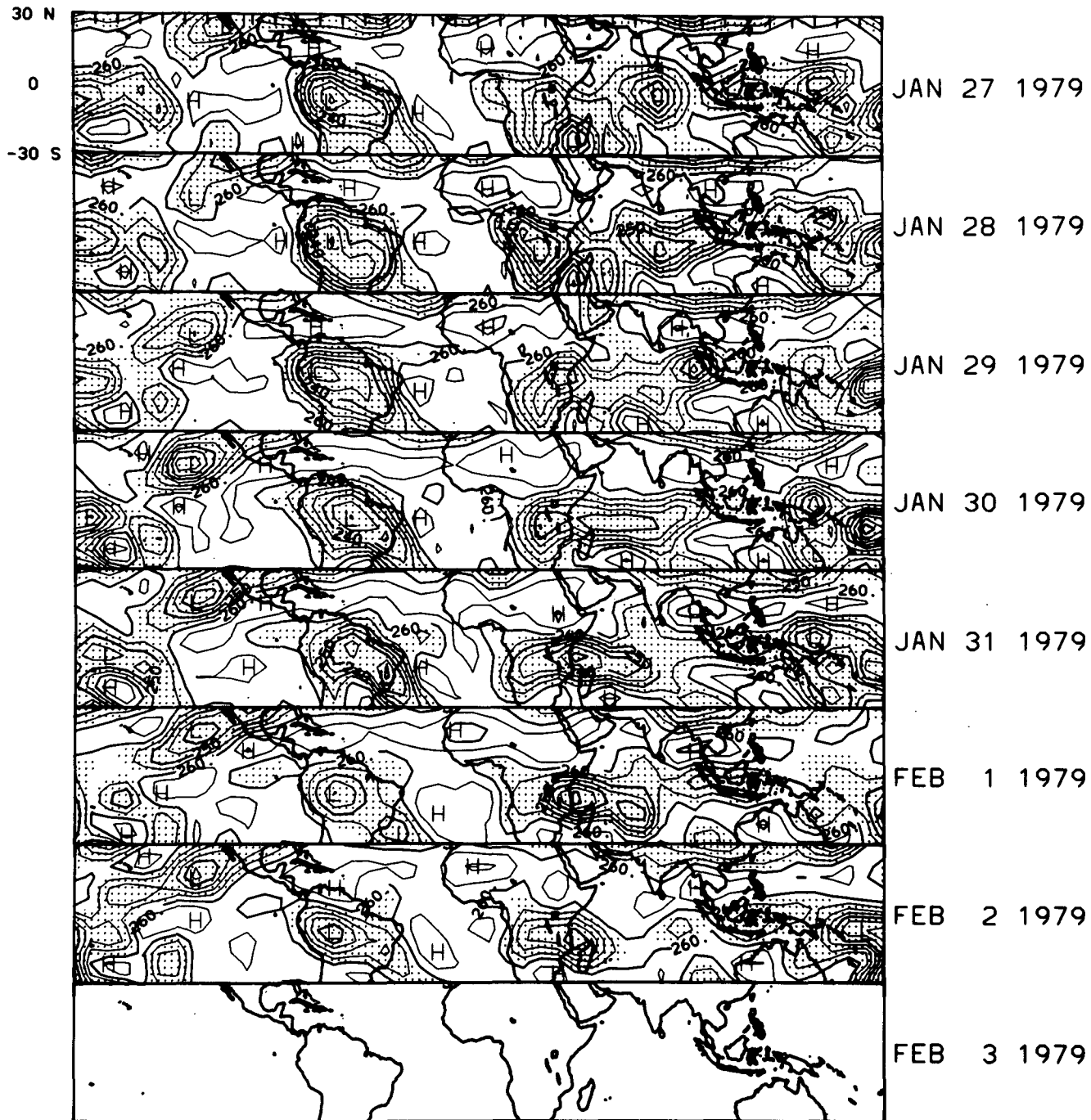
FIG. 20. Time series of the daily IR temperature from the TIROS-N between 30°N and 30°S during the SOP-I study period. Contour intervals are 5 K. Areas colder than 258 K are stippled.

the Amazon Basin is consistent with the time variation of the IR temperatures over the same region, the day-to-day variations of the diagnosed heating rates appear to be more variable as compared with the rather steady appearance of the IR temperature changes.

The temporal variation of heating over Africa between 31 January and 5 February is also discussed in section 3. A similar feature can be seen over the same area in Fig. 19, although here the heating over the western Indian Ocean appears to be more stationary. The temporal variations of IR temperatures in Fig. 20 appear to support the high variability of the ECMWF heating rates in this area. Similarly, the temporal variations of the ECMWF results over the East Indies ap-
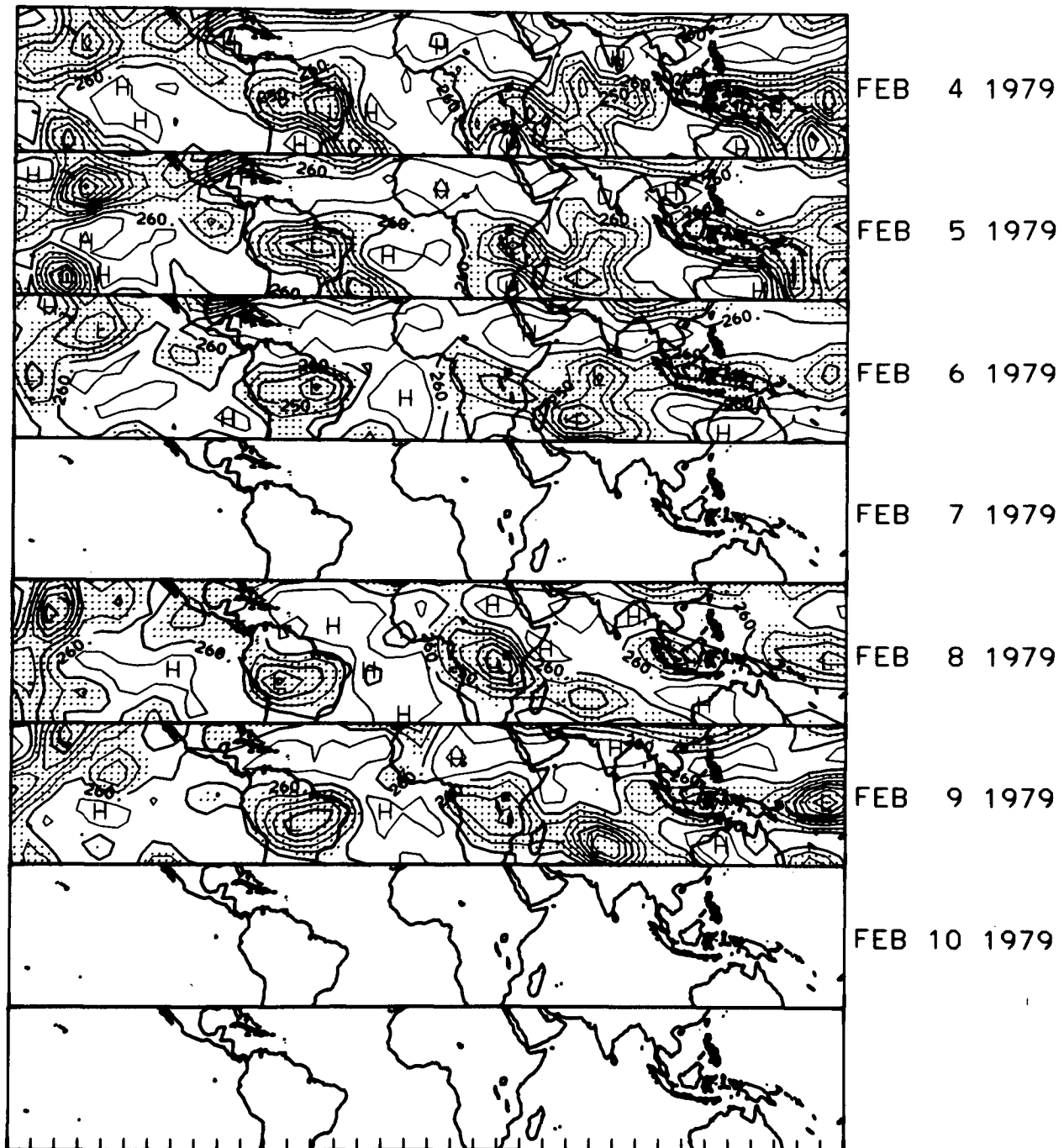
FIG. 20. (*Continued*)

pear in better agreement with that of the IR temperatures than do the temporal variations of the GFDL heating rates. Clearly, we need a more quantitative assessment of the differences between the ECMWF and GFDL diagnosed heating rates together with a quantitative comparison of the GFDL heating rates with the satellite imagery data. This is, however, beyond the scope of the present study and it will be a subject of later report.

REFERENCES

Arkin, P. A., 1979: The relationship between fractional coverage of high cloud and rainfall accumulations during GATE over the B-scale array. *Mon. Wea. Rev.,* **107,** 1382–1387.

——, 1984: An examination of the Southern Oscillation in the upper tropospheric tropical and subtropical wind field. Ph.D. thesis, Department of Meteor., University of Maryland, 240 pp.

Bengtsson, L., 1981: Current problems in four-dimensional data assimilation. *Seminar 1980 on Data Assimilation Methods,* Eu-

ropean Centre for Medium Range Weather Forecasts, 195–217. [Available from ECMWF, Shinfield Park, Reading, U.K.]

Boer, G. J., 1986: A comparison of mass and energy budgets from two FGGE datasets and a GCM. *Mon. Wea. Rev.,* **114,** 885–902.

——, and N. E. Sargent, 1985: Vertically integrated budgets of mass and energy for the globe. *J. Atmos. Sci.,* **42,** 1592–1613.

Chen, T.-C., and W. E. Baker, 1986: Global diabatic heating during FGGE SOP-1 and SOP-2. *Mon. Wea. Rev.,* **114,** 2578–2589.

Daley, R., 1985: The analysis of synoptic scale divergence by a statistical interpolation scheme. *Mon. Wea. Rev.,* **113,** 1066–1079.

Dickson, R. R., 1979: Weather and circulation of February 1979. *Mon. Wea. Rev.,* **107,** 624–630.

Errico, R. M., 1983: *A Guide to Transform Software for Nonlinear Normal Mode Initialization of the NCAR Community Forecast Model.* NCAR Tech. Note, TN-217+1A, 73 pp. [Available from NCAR, Boulder, CO 80307-3000.]

Gill, A. E., 1980: Some simple solutions for heat-induced tropical circulation. *Quart. J. Roy. Meteor. Soc.,* **106,** 447–462.

Girard, C., and M. Jarraud, 1982: Short and medium range forecast differences between a spectral and grid point model. An extensive quasi-operational comparison. Tech. Rep. No. 32, European Centre for Medium Range Weather Forecasts. 176 pp. [Available from ECMWF, Shinfield Park, Reading, U.K.]

Goody, R. M., 1964: *Atmospheric Radiation I, Theoretical Basis.* Oxford, 436 pp.

Griffith, C. G., W. L. Woodley, P. G. Grube, D. W. Martin, J. Stout and D. N. Sikdar, 1978: Rain estimation from geosynchronous satellite imagery-visible and infrared studies. *Mon. Wea. Rev.,* **106,** 1153–1171.

Gruber, A., and A. F. Krueger, 1984: The status of the NOAA outgoing longwave radiation dataset. *Bull. Amer. Meteor. Soc.,* **65,** 958–962.

Heckley, W. A., 1985: The performance and systematic errors of the ECMWF tropical forecasts. Tech. Rep. No. 53, European Centre for Medium Range Weather Forecasts. [Available from ECMWF, Shinfield Park, Reading, U.K.]

Hollingsworth, A., D. B. Shaw, P. Lönnberg, L. Illari, K. Arpe and A. J. Simmons, 1986: Monitoring of observation and analysis quality by a data assimilation system. *Mon. Wea. Rev.,* **114,** 861–879.

Holopainen, E., and C. Fortelius, 1986: Accuracy of estimates of atmospheric large-scale energy flux divergence. *Mon. Wea. Rev.,* **114,** 1910–1921.

Johnson, D. R., R. D. Townsend and M.-Y. Wei, 1985: The thermally coupled response of the planetary-scale circulation to the global distribution of heat sources and sinks. *Tellus,* **37A,** 106–125.

Julian, P. R., 1984: Objective analysis in the tropics: A proposed scheme. *Mon. Wea. Rev.,* **112,** 1752–1767.

——, 1985: Some comparisons of ECMWF IIIb and GFDL IIIb analyses in the tropics. *Proc. First National Workshop on the Global Weather Experiment.* Vol. I, National Academy Press, 211–216.

Kasahara, A., 1982: Nonlinear normal mode initialization and the bounded derivative method. *Rev. Geophys. Space Phys.,* **20,** 385–397.

——, and A. P. Mizzi, 1984: Temporal variations of the divergence field in the ECMWF Level III-b analysis data. *Glob. Wea. Exp. Newslett.,* **7,** 15–21.

——, and ——, 1985: Preliminary evaluation of diabatic heating distribution from FGGE Level IIIb analysis data. *Proc. of the First National Workshop on the Global Weather Experiment,* National Academy Press, Vol. 2, Part I, 317–329.

Kousky, V. E., and M. A. Gan, 1981: Upper tropospheric cyclonic vortices in the tropical South Atlantic. *Tellus,* **33,** 538–551.

Krishnamurti, T. N., and Y. Ramanathan, 1982: Sensitivity of the monsoon onset to differential heating. *J. Atmos. Sci.,* **39,** 1290–1306.

——, S. Cooke, R. Pasch and S. Low Nam, 1983: Precipitation estimates for rain gauge and satellite observations. Florida State University Rep. No. 83-7, Dept. of Meteor., Florida State University, Tallahassee, FL, 373 pp.

Lorenc, A. C., 1984: The evolution of planetary-scale 200 mb divergent flow during the FGGE year. *Quart. J. Roy. Met. Soc.,* **110,** 427–441.

Masuda, K., 1984: Diabatic heating during the FGGE: A preliminary report. *J. Meteor. Soc. Japan,* **62,** 702–708.

Mohanty, U. C., R. P. Pearce and M. Tiedtke, 1984: Numerical experiments on the simulation of the 1979 Asian summer monsoon. Tech. Rep. No. 44, European Centre for Medium Range Weather Forecasts. 44 pp. [Available from ECMWF, Shinfield Park, Reading, U.K.]

——, A. Kasahara and R. Errico, 1986: The impact of diabatic heating on the initialization of divergent circulations in a global forecast model. *J. Meteor. Soc. Japan,* **64,** 805–817.

Murakami, M., 1983: Analysis of the deep convective activity over the western Pacific and southeast Asia. Part I: Diurnal variation. *J. Meteor. Soc. Japan,* **61,** 60–76.

——, 1984: Analysis of the deep convective activity over the western Pacific and southeast Asia. Part II: Seasonal and intraseasonal variations during northern summer. *J. Meteor. Soc. Japan,* **62,** 88–108.

Murakami, T., and Y.-H. Ding, 1982: Wind and temperature changes over Eurasia during the early summer of 1979. *J. Meteor. Soc. Japan,* **60,** 183–196.

Newell, R. E., D. G. Vincent, T. G. Dopplick, D. Ferruzza and J. W. Kidson, 1969: The energy balance of the global atmosphere. *The Global Circulation of the Atmosphere,* G. A. Corby, Ed., Royal Meteor. Soc., London, 42–90.

Paegle, J., and W. E. Baker, 1982: Planetary-scale characteristics of the atmospheric circulation during January and February 1979. *J. Atmos. Sci.,* **39,** 2521–2538.

Platt, C. M., 1983: On the bispectral method for cloud parameter determination from satellite VISSR data: Separating broken cloud and semitransparent cloud. *J. Climate Appl. Meteor.,* **22,** 429–439.

Puri, K., 1985: Sensitivity of low-latitude velocity potential field in a numerical weather prediction model to initial conditions, initialization and physical processes. *Mon. Wea. Rev.,* **113,** 449–466.

Reiter, E. R., and D.-Y., Gao, 1982: Heating of the Tibetan Plateau and movements of the south Asian high during spring. *Mon. Wea. Rev.,* **110,** 1694–1711.

Richards, F., and P. Arkin, 1981: On the relationship between satellite-observed cloud cover and precipitation. *Mon. Wea. Rev.,* **109,** 1081–1093.

Sato, R., L. M. Bath, D. L. Williamson and G. Williamson, 1983: *Users' Guide to NCAR CCM0B.* NCAR Tech. Note TN-211+1A. [Available from NCAR, Boulder, CO 80307-3000.]

Schubert, S. D., and G. F. Herman, 1981: Heat balance statistics derived from four-dimensional assimilations with a global circulation model. *J. Atmos. Sci.,* **38,** 1891–1905.

Stern, W. F., J. J. Ploshay and K. Miyakoda, 1985: Continuous data assimilation at GFDL during FGGE. *Seminar/Workshop 1984, Data Assimilation Systems and Observing System Experiments with Particular Emphasis on FGGE.* Vol. 2, 125–156. [Available from ECMWF, Shinfield Park, Reading, U.K.]

Stout, J. E., D. W. Martin and D. N. Sikdar, 1979: Estimating GATE rainfall with geosynchronous satellite images. *Mon. Wea. Rev.,* **107,** 585–598.

Virji, H., 1981: A preliminary study of summertime tropospheric circulation patterns over South America estimated from cloud winds. *Mon. Wea. Rev.,* **109,** 599–610.

Wei, M.-Y., D. Johnson and R. D. Townsend, 1983: Seasonal distributions of diabatic heating during the First GARP Global Experiment. *Tellus,* **35A,** 241–255.

Williamson, D. L., 1983: *Description of the NCAR Community Climate Model (CCM0B).* NCAR Tech. Note TN-210+STR, 88 pp. [Available from NCAR, Boulder, CO 80307-3000.]

——, L. M. Bath, R. K. Sato, T. A. Mayer and M. L. Kuhn, 1983: *Documentation of NCAR CCM0B program modules.* NCAR Tech. Note TN-212+1A. [Available from NCAR, Boulder, CO 80307-3000.]